Multiscale FEM-DEM model for spontaneous droplet digging in a hot granular bed

Michel Henry [a,*], Nathan Coppin [a,c], Stéphane Dorbolo [b], Vincent Legat [a], Jonathan Lambrechts [a]

[a] *Institute of Mechanics, Materials and Civil Engineering, Applied Mechanics and Mathematics, Avenue Georges Lemaitre 4-6 bte L4.05.02, Louvain-la-Neuve, Belgium*
[b] *FNRS-CESAM-Soft Matter-PtyX, Département de Physique B5, Allée du 6 aout, 19, 4000 Liège, Belgium*
[c] *Laboratoire de Mécanique et Génie Civil, Montpellier, 34090, France*

ARTICLE INFO

ABSTRACT

Fluidised granular beds are used in a variety of industrial applications, such as heat exchangers, chemical reactors and energy storage systems. Fluidisation increases the interaction surface between the grains and the fluid, thus improving heat transfer. In this paper, an unresolved/semi-resolved FEM-DEM model is introduced to simulate immersed granular flows, incorporating heat transfer and vaporisation. As the fluid is modelled using a volume-averaged approach, constitutive laws are introduced to represent the momentum and heat transfer between the grains and the fluid. Based on the Colburn–Reynolds analogy, a Nusselt correlation is proposed to quantify the heat transfer of an assembly of grains within a fluid. The proposed law is validated by experimental measurements of heated granular beds taken from the literature. Heat transfer in a bubbling fluidised bed is studied as a numerical benchmark. The spontaneous digging of a droplet of water in a hot granular bed is investigated. When a droplet of water is placed on the surface of a hot granular bed, depending on the granular temperature, it can dig spontaneously into the bed. The main trends of the experiment, namely digging, local fluidisation and the formation of a chimney, are reproduced by the simplified two-dimensional numerical model. Heat transfer during the excavation process is investigated to highlight efficient transfer due to the local fluidisation. It is demonstrated that both injection fluidisation and local vaporisation fluidisation are correctly captured, as is heat transfer between the different phases.

1. Introduction

Fluidised bed reactor is a dynamic multiphase process: a fluid is injected through a granular material. The procedure is mainly used to extract chemical products from the granular material or to purify the fluid phase. Fluidisation is also a promising process to extract energy from a granular bed [1]. The granular material, when fluidised, provides a large surface area for interaction. Taking advantage of the low thermal conductivity of the granular material, energy not used by the grid can be store in a sand silo by heating grains. Once energy is needed, the heat can be released by injecting water through pipes crossing the sand assemble to produce steam. Recently, a new fluidisation process has been observed using liquid droplets which dig into a granular bed [2]. This process allows a better exploitation of the heat contained in the silo. On an industrial scale, circulating fluidised bed boilers implement this process. Heat is generated by combustion and efficiently transported by injecting a fluid in the granular bed. Two kinds of particles are present in the bed, the bed particles, usually sand or ash, and the fuel particles, coal or biomass. Depending on the

injecting flow, various regimes can be observed: percolation, bubbling, fast fluidisation, turbulent fluidisation and pneumatic regime. The most common regimes used in the industry are bubbling fluidised bed and fast fluidised bed [3]. In these cases, the fluidisation is obtained by injecting a fluid at a velocity higher than the minimum fluidisation velocity. The bubbling regime is characterised by the presence of bubbles which carry particles in their wake. The suspension becomes heterogeneous. The solid packing fraction decreases quickly close to the bubbles but remains large in the rest of the bed. The fast fluidised regime, obtained for higher fluid velocity, is characterised by particle recirculation within the granular medium which tends to uniformise the solid packing fraction across the suspension. As the efficiency of the process is highly dependent on the fluidisation regime, studying heat transfer inside the granular material is essential to optimise the process.

A recent observation has suggested an alternative fluidisation process using digging droplet . When a drop of water is released on a

---

hot granular bed, depending on the temperature of the granular bed, the drop can either crash on the interface, spontaneously dig into the granular bed, or levitate over it. At a temperature close to the vaporisation temperature, the droplet collapses onto the granular bed. Heat is transferred to the grains over a short period of time and only at the top of the granular bed. At higher temperatures, the thrust of the vapour expelled from the droplet is sufficient to sustain the droplet isolated above the grains. This phenomenon is called the Leidenfrost effect [4,5]. Another effect of the vapour is to locally fluidise an area of the bed below the droplet. The droplet and its surrounding film of vapour enter the fluidised region and begin to dig progressively. In this regime, heat transfer is maximal as heat is released within the granular bed and the temperature gradient is maintained by the recirculation of the grains. At very high temperatures, the thrust is sufficient to prevent the droplet from entering the fluidised zone. Heat transfer is reduced as it only occurs at the top of the bed.

The interaction between a liquid droplet and a hot granular material is challenging as the thermal exchanges are complex due tot he granular contact network and the droplet shape. In the regimes considered, the water undergoes a phase change which add complexity to the problem. Modelling this situation is highly challenging but necessary to better understand of both the Leidenfrost state and the thermal properties of the granular materials. Over the last decades, many methods have been developed to understand granular suspension flows [6,7]. We use a discrete element method (DEM) for the grains coupled with a classical computational fluid dynamics (CFD) method for the fluid phase using volume-averaged equations [8]. Compared to a two-fluid approach, where both the grains and the fluid are represented as continuous phases [9], CFD-DEM allows to explicitly represent interactions between grains [10,11]. The spatial resolution of the fluid phase can be adjusted as a compromise between computational cost and accuracy. Fully resolved methods have a fluid resolution smaller than the grains and capture the boundary layer around them. Semi-resolved and unresolved methods have a fluid resolution of the same order or larger than the grains. Constitutive laws are required to couple the exchange between the two phases [12,13]. In recent years, these methods have been used to investigate heat transfer in fluidised granular flows [14,15]. While drag correlation for immersed granular flows are well-established, the ones for heat transfer is not yet unified [16–19].

We propose a multi-scale model to study the heat transfer of a granular bed fluidised by injection from below and droplet deposition from above. The mesh size varies from a semi-resolved approach around the droplet to an unresolved approach away from the droplet. We present and validate a correlation model for heat transfer across percolating and bubbling regimes [20,21]. The numerical model is then extended to study the heat transfer between a drop and a granular bed, taking into account vaporisation. We investigate the spontaneous digging of the drop in a two-dimensional granular bed, highlighting the conditions under which this digging occurs. Finally, we study the efficiency of heat transfer in different regimes to discuss the potential applications of this phenomenon.

2. Multi-scale model

In the following first sub-section, the volume-averaged Navier–Stokes equations (VANS) are introduced to model the fluid phase [8]. This choice ensures a reasonable computational cost while capturing the global flow behaviour. In the Section 2, the solid phase is described by the discrete element method (DEM). It is assumed that each grain is tracked individually as a rigid body with a given mass, velocity, and temperature. As the fluid resolution scale is larger than the boundary layer formed around the grains, constitutive laws have to be introduced to model momentum and heat transfer between the fluid and the particles. The Section 3 is dedicated to the particle–fluid interaction constitutive laws. The multi-scale representation of the flow is illustrated in Fig. 1. The numerical implementation is
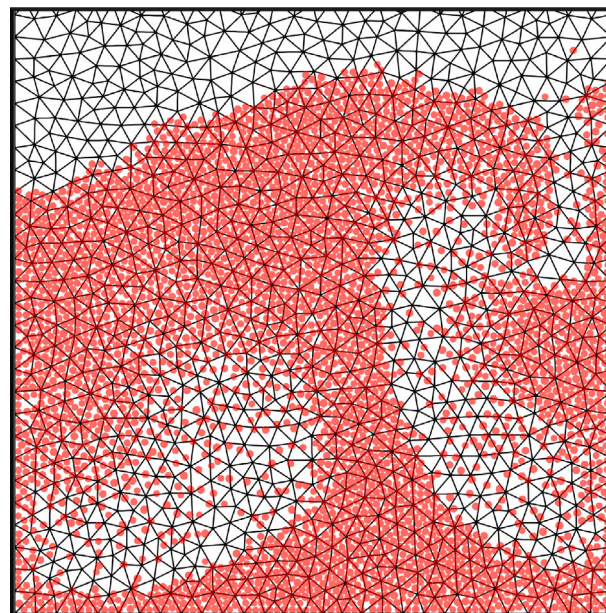

Fig. 1. Immersed granular flow representation. The fluid phase is described by the volume-averaged Navier–Stokes equations captured at the mesh scale. The discrete element method models the particles, represented by the red discs. (For interpretation of the references to colour in this figure legend, the reader is referred to the web version of this article.)

conducted using the open-source solver MigFlow[1] [12,22–25]. The fluid phase is solved using the classical finite element method, while the solid phase is handled with the discrete element method. The fluid's spatial discretisation is achieved through a stabilised $\mathbb{P}_1 - \mathbb{P}_1$ mixed formulation. Particle collisions are addressed using the non-smooth contact dynamics approach [26]. Appendix B provides an overview of the contact dynamics including heat transfer. To maintain stability between the two solvers, a semi-implicit time integration scheme is used [12].

2.1. Fluid phase

To represent the particles presence in the fluid, three aspects have to be considered, the governing equations, the numerical scheme and the particle–fluid interaction forces. The governing equations are obtained through a local average of the Navier–Stokes equations based on the work of Anderson [8]. The equations are expressed in terms of averaged quantities over a control volume with a fluid volume fraction ϵ. The flow is described at a macroscopic scale and constitutive laws must be introduced to model particle-force interaction. From the averaged equations, three sets of equations can be derived as pointed out by Zhou [27]. They differ by the way the fluid–particle interaction force is incorporated into the momentum equation. Set I corresponds to the one obtained only assuming the averaging process. Set II is obtained by decomposing the stress tensor into a macroscopic and a microscopic part. Set III used the same decomposition and a continuous representation of the solid phase to eliminate the fluid stress tensor in the momentum equation of the solid phase. For a detailed analysis of each set, the reader is referred to the work of Zhou [27] and analysis of Feng [28]. In this work, set I is used to model the fluid phase. The numerical scheme and spatial discretisation of the particle–fluid interaction are detailed in Appendix A. The flow is assumed to be incompressible and natural convection is captured by the Boussinesq approximation. All other material properties are assumed to be independent of temperature. It leads

---

[1] https://www.migflow.be.

to the following volume-averaged Navier–Stokes (VANS) equations in their non-conservative form,

$$\frac{\partial \epsilon}{\partial t} + \boldsymbol{\nabla} \cdot (\epsilon \boldsymbol{u}) = 0, \tag{1}$$

$$\epsilon \rho \, \frac{\mathrm{d}\boldsymbol{u}}{\mathrm{d}t} = \boldsymbol{\nabla} \cdot \boldsymbol{\sigma} + \boldsymbol{f}_p + \left(1 + \beta \left(T - T_R\right)\right) \epsilon \rho \boldsymbol{g}, \tag{2}$$

$$\epsilon \rho c \, \frac{\mathrm{d}T}{\mathrm{d}t} = -\boldsymbol{\nabla} \cdot \boldsymbol{q} + q_p, \tag{3}$$

where ρ is the fluid density, c the specific heat at constant volume, β the thermal expansion coefficient and T_R the reference temperature. The $\frac{\mathrm{d}\bullet}{\mathrm{d}t} = \frac{\partial \bullet}{\partial t} + \boldsymbol{u} \cdot \boldsymbol{\nabla}\bullet$ operator denotes the material derivative. The stress tensor $\boldsymbol{\sigma}$ is modelled as

$$\boldsymbol{\sigma} = -p\boldsymbol{I} + \epsilon \eta \left(\boldsymbol{\nabla}\boldsymbol{u} + \boldsymbol{\nabla}^T\boldsymbol{u}\right)$$

where p is the pressure, $\boldsymbol{I}$ is the identity tensor and η is the dynamic viscosity. A modified Fourier's law is used to model the heat flux density $\boldsymbol{q}$ as

$$\boldsymbol{q} = -\epsilon k \boldsymbol{\nabla} T$$

where k is the thermal conductivity. The momentum transfer and the heat transfer exerted by the particles on the fluid are denoted by $\boldsymbol{f}_p$ and q_p respectively. The force density incorporates both the averaged stress tensor contribution and the boundary layer contribution. The latter only accounts for the drag force, neglecting other forces such as the Basset force or virtual mass effects. The force density contribution exerted by the particles on the fluid is given by

$$\boldsymbol{f}_p = \begin{cases} -\boldsymbol{\nabla} \cdot \boldsymbol{\sigma} + \boldsymbol{f}_d, & \boldsymbol{x} \in \mathcal{P} \\ \boldsymbol{0}, & \text{elsewhere} \end{cases} \tag{4}$$

where $\boldsymbol{f}_d$ represents the drag force density and $\mathcal{P}$ the domain occupied by particles. Similarly, the heat transfer density is given by

$$q_p = \begin{cases} \boldsymbol{\nabla} \cdot \boldsymbol{q} + q_c, & \boldsymbol{x} \in \mathcal{P} \\ 0, & \text{elsewhere} \end{cases} \tag{5}$$

where q_c is the forced convection due to the boundary layer around the grain. In pratice, at the grain scale, both the viscous stress and heat flux are negligible compared to the net force and to the forced convection. The parametrisation of the drag force and the forced convection are detailed in Section 2.3.

2.2. Solid phase

As each particle is modelled as a rigid body, the motion of a particle is governed by Newton's second law and its temperature by the energy conservation equation.

$$\rho \, \frac{\mathrm{d}\boldsymbol{v}}{\mathrm{d}t} = \boldsymbol{f}_c - \boldsymbol{f}_p + \rho \boldsymbol{g} \tag{6}$$

$$\rho c \, \frac{\mathrm{d}T}{\mathrm{d}t} = q_c - q_p \tag{7}$$

where ρ is the particle density, $\boldsymbol{v}$ is the particle velocity, $\boldsymbol{g}$ is the gravity vector and $\boldsymbol{f}_c$ is the contact force density. The particle temperature is denoted by T, c is the particle specific heat and q_c is the heat transfer density due to the collisions.

2.3. Constitutive laws

As the boundary layer is not captured by the fluid resolution scale, constitutive laws are introduced to model its interaction with the particles. Momentum and heat transfer are modelled by correlations of their respective dimensionless numbers. The drag force is scaled by the dynamic pressure and the cross-sectional area of the sphere A, leading to the definition of the drag coefficient C_d. The forced convection is scaled by the conductive heat transfer and the surface area of the sphere S, which gives the Nusselt number Nu. These dimensionless numbers are defined as

$$\frac{f_d}{\frac{1}{2}\rho \|\boldsymbol{v} - \boldsymbol{u}\|^2} \frac{V}{A} = C_d, \qquad \frac{q_c \, d}{k(T_p - T)} \frac{V}{S} = \text{Nu}. \tag{8}$$

where V is the volume of the sphere. Correlations have to be valid depending on the flow regime which is characterised by the fluid volume fraction ϵ and the Reynolds number Re. Heat transfer also depends on the relative thickness of the momentum and thermal boundary layers, which is described by the Prandtl number Pr. These two dimensionless numbers are defined as

$$\text{Re} = \frac{\rho d \|\boldsymbol{v} - \boldsymbol{u}\|}{\eta}, \qquad \text{Pr} = \frac{c\eta}{k}.$$

As transport mechanisms are gathered by the same eddies for heat and momentum transfer, these two transfer can be correlated by the Reynolds–Colburn analogy [29],

$$\text{Nu} \propto C_f \text{Re} \text{Pr}^{\alpha}. \tag{9}$$

where C_f is the skin friction coefficient, which accounts solely for viscous stress, while the drag coefficient encompasses both viscous stress and pressure contributions. This analogy does not strictly hold across all flow regimes, as the thermal boundary layer also depends on the momentum boundary layer. However, it offers a useful starting point for adjusting heat transfer correlations based on momentum transfer correlations. By relating the drag coefficient to the skin friction coefficient, Duan & Duan [30] proposed a correlation for the Nusselt number of a single sphere,

$$\text{Nu} \approx f(\text{Re}) \frac{C_d \text{Re}}{12} \text{Pr}^{\alpha}, \qquad f(\text{Re}) = \frac{\text{Re} + \delta}{0.11 \text{Re}^{1.4} + \text{Re} + \delta}. \tag{10}$$

Discrepancies in the analogy are modelled by the function $f(\text{Re})$, with the Prandtl exponent set to $\alpha = 0.4$. The δ value within $f(\text{Re})$ is adjusted from the one proposed by Duan & Duan, reducing it from $\delta = 5000$ to $\delta = 500$ for better alignment with experimental data at intermediate Reynolds numbers. To extend this correlation to an assembly of spheres, the influence of neighbouring particles must be considered. The methodology used to extend the drag force to an assembly is also applied to forced convection. The drag force on a sphere within an assembly is obtained by multiplying the drag force for a single sphere by the voidage function $g(\epsilon, \text{Re})$ and using the superficial Reynolds number instead of the Reynolds number. In this work, the voidage function proposed by Di Felice [31,32] is used,

$$g(\epsilon, \text{Re}) = \epsilon^{-1.8 + \exp\left[-\dfrac{(1.5 - \log \text{Re})^2}{2}\right]}, \tag{11}$$

and the drag coefficient correlation is the one proposed by Dallavalle [33]. It results in the following drag coefficient and Nusselt correlations for a sphere in an assembly

$$C_d \approx g(\epsilon, \text{Re}) \left(0.63 + \frac{4.8}{\sqrt{\epsilon \text{Re}}}\right)^2, \tag{12}$$

$$\text{Nu} \approx g(\epsilon, \text{Re}) \, f(\epsilon \text{Re}) \left(0.18 \sqrt{\epsilon \text{Re}} + 1.39\right)^2 \text{Pr}^{0.4}. \tag{13}$$

The proposed Nusselt correlation is compared with a collection of experimental data from the literature [20] in Fig. 2. The experiment measures heat transfer through a heated packed bed of spheres. In this dense regime the correlation is found to be in good agreement with the experimental data. As the purpose of the model is to be able to capture local fluidisation, a bubbling fluidised granular bed boiler is studied. Based on the analogy, the Nusselt constitutive law is dependent on the one used for the drag coefficient. The used drag correlation has been extensively employed in CFD-DEM modelisation of dense monodisperse assembly and fluidised bed reactors. This law has been successfully used to model drag force for different fluid nature such as water or air. Therefore, we expect the Nusselt correlation to be valid for these fluids as well.

Table 1
Parameters used for the fluidisation of a heated packed bed.

| Fluid properties			Grain properties		
Density ρ	kg m^{-3}	1.204	Density ρ	kg m^{-3}	2500
Viscosity η	kg m^{-1} s^{-1}	2 10^{-5}	Heat capacity c	J kg^{-1} K^{-1}	840
Heat capacity c	J kg^{-1} K^{-1}	1010	Heat conductivity k	J s^{-1} m^{-1} K^{-1}	1.4
Heat conductivity k	J s^{-1} m^{-1} K^{-1}	0.025	Young's modulus E	kg m s^{-1}	6 10^{10}
Thermal expansion β	K^{-1}	0.003	Poisson's ratio v	\	0.22
			Dry friction μ	\	0.3
Geometry properties			Boundary parameters		
Height h	cm	25	Inflow velocity $\hat{v}$	m s^{-1}	1.2, 1.54, 1.71
Width w	cm	8	Inflow temperature $\hat{T}$	K	290
Thickness p	cm	1.5	Wall temperature $\hat{T}_w$	K	290
Nozzle l	cm	1.2			
Grain diameter d	mm	1			
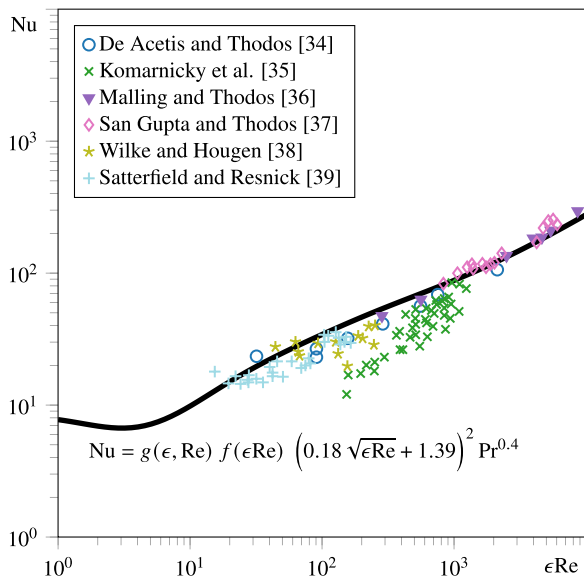
Fig. 2. Nusselt number correlation of a sphere in a dense assembly. The black curve refers to the proposed correlation in Eq. (13) with a fluid volume fraction of $\epsilon = 0.45$. The markers refers to experimental data collected by Wakao [20] (see [34–39]).

3. Bubbling fluidised granular bed boiler

In this section, the model is validated in the context of a fluidised bed based on the experiment proposed by Patil [21]. The bubbling regime is obtained by the injection of air at a sufficiently high velocity at the bottom of the container. The heat transfer between the particles and the fluid is driven by the bubble dynamics and the exchange at its boundary. Once a bubble arises through the particles bed, it drags particles along its path which reduces the local solid fraction. This motion allows the air to invade the bed and cool the particles. To validate the heat transfer model in this transient regime, an equivalent two-dimensional model is proposed and validated against the experimental data.

Two-dimensional simulations are performed based on a pseudo-2D bubbling fluidised bed. Fig. 3 illustrates the geometry of the problem. The granular bed consists of hot spherical glass beads immersed in air initially at rest. Side walls at constant temperature $\hat{T}_w$ cool down the bed. At the bottom, a porous plate enables fluidisation by the injection of air at a prescribed flow velocity $\hat{u} = (0, -\hat{v}, 0)$. The injected air forms bubbles that rise through the bed, ejecting particles along the way. A nozzle blocks the flow in the centre of the bottom plate. To avoid cristallisation, the diameter of the beads is uniformly distributed between $0.8d$ and d. Table 1 describes the physical and the geometry parameters used for the simulations.

3.1. Numerical considerations

Due to the multi-scale nature of the model, the boundary layer is not fully resolved close to the wall. The heat transfer associated with these conditions is assumed to follow a Newton's law $q_w = \frac{h_w}{h}\left(\hat{T}_w - T\right)$ and its convection coefficient is set to be equivalent to the one used in the reference experiment by Patil [21], $h_w = 350$ [W m^{-2} K^{-1}]. The simulation is performed on a two-dimensional domain instead of a three-dimensional Hele-Shaw cell. Since the viscous effects damping the fluid flow and the forced convection in the vicinity of the front and rear walls are not captured, a volumetric drag force and a volumetric heat transfer model these longitudinal effects,

$$\boldsymbol{f}_l = -\gamma\boldsymbol{u}, \qquad\qquad q_l = \lambda(\hat{T}_w - T). \qquad (14)$$

These two coefficients must be calibrated to reproduce experimental data. As suggested in [22], the drag coefficient is estimated by considering a Hagen–Poiseuille flow. The drag coefficient is assumed to be $\gamma = 12\mu/p^2$. Its value in these experiments is set to $\gamma \approx 1.067$ [kg m^{-3} s^{-1}]. The heat transfer coefficient is estimated by comparing the averaged particle temperature with the experimental data for an inflow velocity of $\hat{v} = 1.54$ [m/s] and the mass bed of $m = 75$ [g]. The estimated heat transfer coefficient is found to be $\lambda \approx 4\ 10^4$ [W m^{-3} K^{-1}]. All these parameters have been calibrated with a static friction coefficient between two particles as $\mu_s = 0.3$ and a coefficient of $\mu_s = 0.5$ between a particle and the wall. As long as the friction coefficient is non-zero, its impact on the dynamics of the bed is expected to be limited. Describing the beads as discs rather than spheres tends to underestimate their mobility, a disc has only 3 degrees of freedom whereas a sphere has 6 of them. In order to reproduce the same packing fraction and a similar mobility as in the three-dimensional case, the grains are assumed to be porous to reach the jamming packing fraction of a sphere packing. The jamming packing fraction of a disc packing is $\phi_{\max} = 0.9069$ while the jamming packing fraction of a sphere packing is $\phi_{\max} = 0.7405$. The boundary conditions at the walls, inflow and outflow are summarised in the following table, either a Dirichlet or a Neumann condition is applied.

Inflow	Outflow	Lateral wall	Longitudinal wall
$\boldsymbol{u} = \hat{\boldsymbol{u}}$	$\boldsymbol{f} = \boldsymbol{n}\cdot(\boldsymbol{\sigma} - \epsilon\rho\boldsymbol{uu})$	$\boldsymbol{u} = \boldsymbol{0}$	$\boldsymbol{f} = \boldsymbol{f}_l$
$T = \hat{T}$	$q = \boldsymbol{n}\cdot(-\boldsymbol{q} - \rho c\boldsymbol{u}T)$	$q = q_w$	$q = q_l$

3.2. Dynamics

Fig. 4 shows the numerical results of the bed fluidisation by the air injection. As the bubbles rise through the granular bed, they drag particles with them. Due to the symmetry of the problem, a central aisle is naturally generated along which the particles are not dragged because of to the closed nozzle. The cooled particles accumulate at the
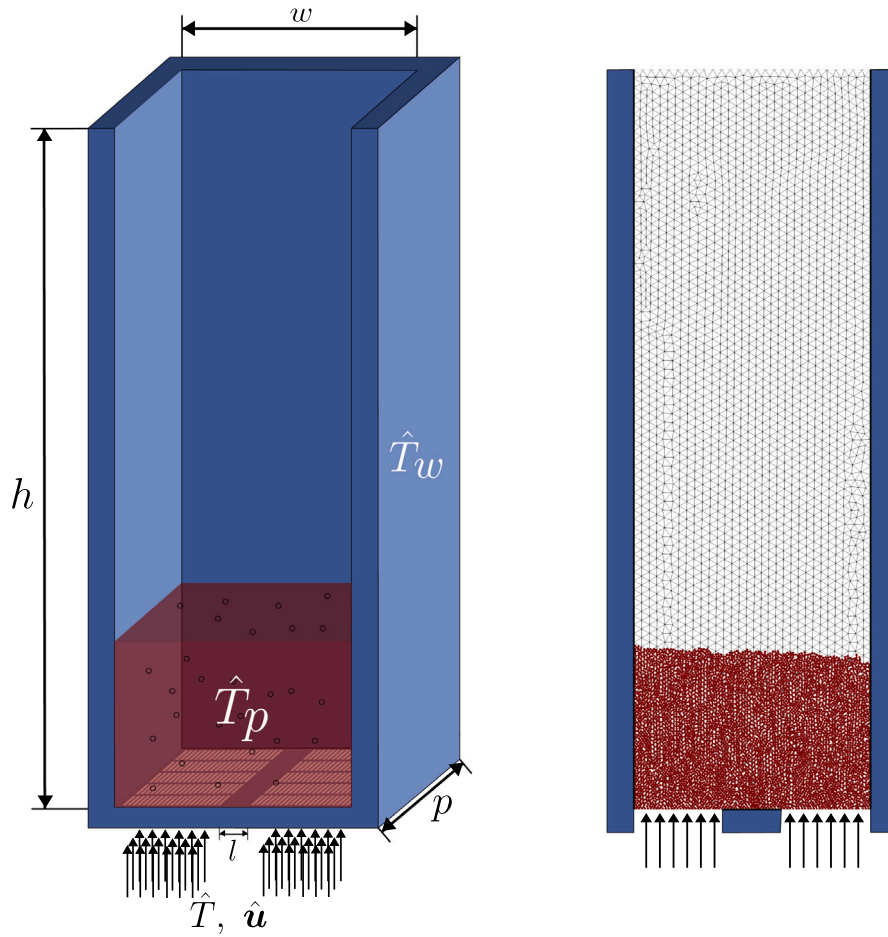
Fig. 3. On the left, schematic of the pseudo-2d bubbling fluidised bed setup. On the right, two-dimensional numerical representation of the problem. Air at a lower temperature than the grains is injected through the bottom porous plate to fluidise the granular bed.
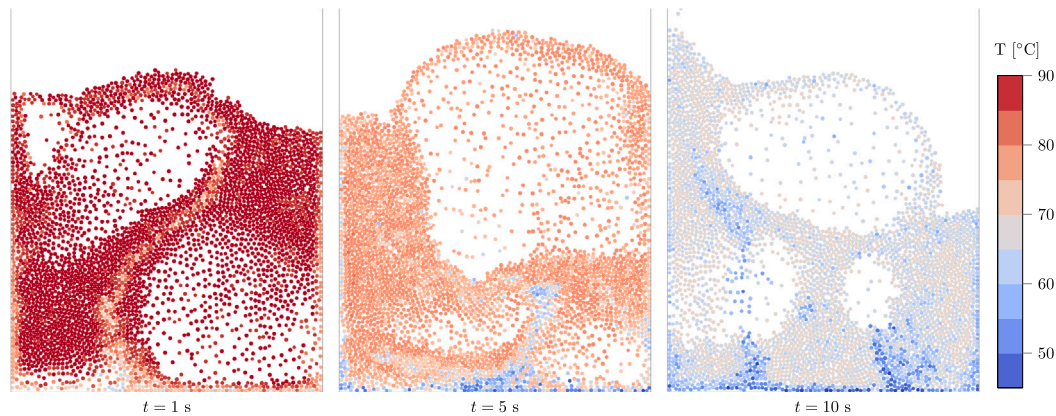

Fig. 4. Snapshots of the particle dynamics at different time for $\bar{v} = 1.71$ [m/s] with a bed mass of $m = 75$ [g]. Particle temperature is represented by the colour map. (For interpretation of the references to colour in this figure legend, the reader is referred to the web version of this article.)

bottom of the bed and are transported away by the convective cells created by the bubbles (see Fig. 5).

Two symmetrical vortices can be seen in the wake of the bubbles. In these vortices, the particle velocity is upward in the centre of the domain and downward at the wall. As pointed out by Yang [40], the preferred path of the bubbles is along the centre of their region, resulting in a higher solid fraction at the edge of the domain (see Fig. 6).

3.3. Heat transfer

As the air flows through the bed, the particles are cooled down. The heat transfer between the particles and the fluid is controlled by the bubble dynamics and the exchange with the boundary. Increasing the inflow velocity increases the heat transfer between the particles and the fluid. Firstly, bubbles are more easily formed which favours particle motion. This movement reduces the local solid fraction allowing air to invade and cool the particles. Secondly, a higher inflow velocity
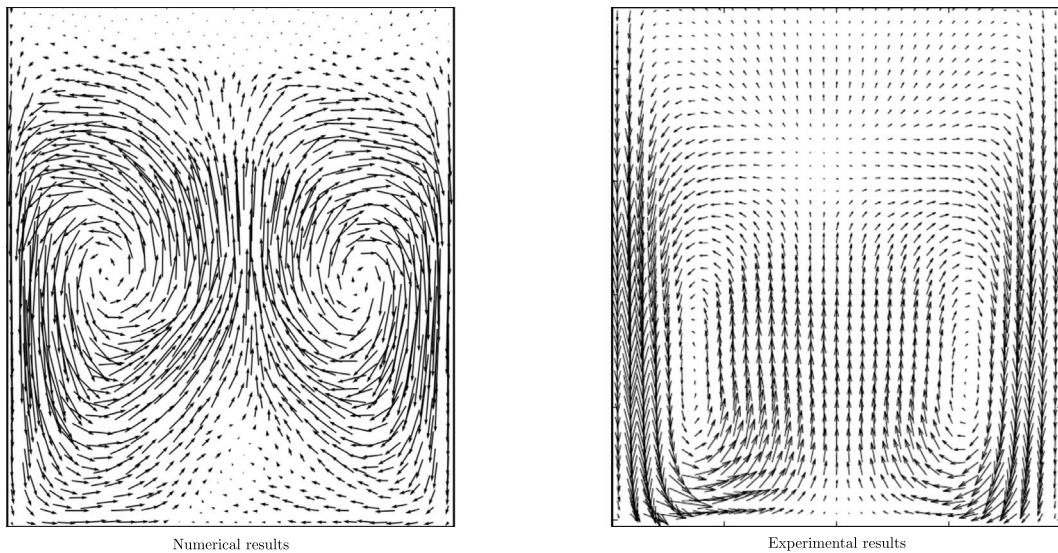
Fig. 5. Time-averaged particle velocity over a time of 5 s starting at a time of 5 [s].
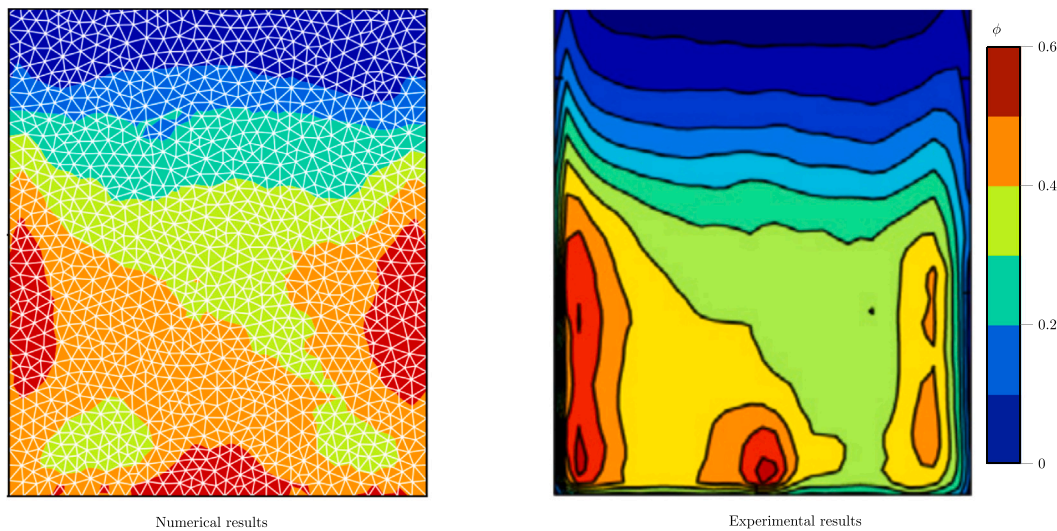

Fig. 6. Time-averaged solid packing fraction over a time of 5 s starting at a time of 5 [s].

increases the heat transfer coefficient. Fig. 7 shows good agreement between the experimental and numerical results of the averaged particle temperature. The fluxes through the front and rear walls are calibrated on the set of measurements with a mass of $m = 75$ [g] and an inflow velocity of $\hat{v} = 1.54$ [m/s] and validated on others inflow velocities. The numerical model proposed on the basis of Eq. (13) is able to reproduce qualitatively and quantitatively the heat transfer between the particles and the fluid. Based on this representation of a bubbling fluidised bed, local fluidisation is expected to be well represented.

4. Spontaneous water droplet digging

When a droplet falls into a hot granular bed, the droplet is able to penetrate the granular medium spontaneously. The spontaneous digging was firstly documented by Lin [2] in a quasi-2D experiment and in a 3D granular bed. In this three-dimensional case, the observations are limited to the grain ejection and to the final stage when the droplet is stopped. Once the droplet is stopped, a cohesive spherical structure can be extracted from the granular bed. In the quasi-2D experiment, the droplet motion and the fluidisation of the granular bed are observed through an Hele-Shaw cell. This cell is in fact quasi

bi-dimensional regarding the droplet motion, the grains being smaller than the droplet can still move in the depth direction. The numerical experiment presented in this work assumes a two-dimensional domain to mimic the experimental setup. However, the constraint in the third direction does not allow a quantitative comparison with the physical experiment. The main phenomena are still present and are investigated in this study.

Different regimes have been observed depending on the droplet's ability to fluidise the granular medium. In the first regime, vaporisation is not sufficient to create a layer of vapour at the interface between the droplet and the granular medium. The droplet crashes into the granular medium, and a small cavity may form but does not deepen. In the second regime, a layer of vapour is created between the droplet and the granular medium. The droplet fluidises the surrounding particles. The grains are ejected into the resulting vertical chimney, and the droplet goes downwards before the granular medium reorganises. The droplet then takes the place of the ejected grains and continues to dig. In that regime, the local fluidisation tends to favorise heat transfer with grains. The main result is that the droplet stops at different depth according to the temperature of the granular material. A maximum depth is found for a temperature between the starting digging temperature and the
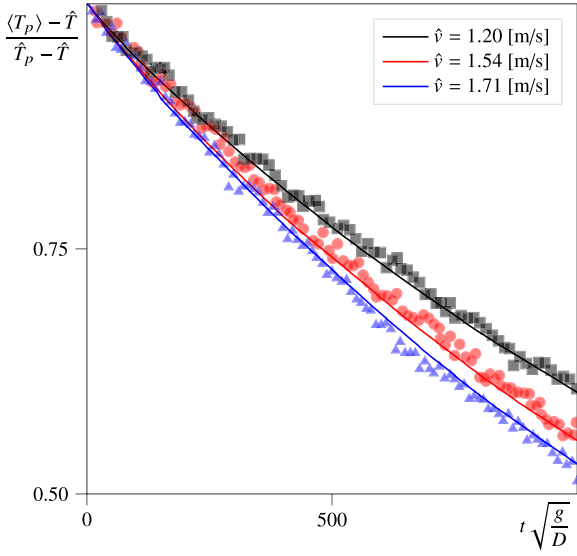
Fig. 7. Mean particle temperature evolution. Experimental values, indicated by markers, have been extracted from [21]. Simulation results are shown by a continuous line for each set of data corresponding to different inflow velocity, respectively, 1.20, 1.54 and 1.71 [m/s].

temperature for which the droplet remains at the surface. In the third regime, at high temperature, the droplet stops digging and is close to the surface. In the following, the droplet dynamics is studied in the second regime, named the digging regime, and to understand the stop of the droplet at high temperatures.

The numerical simulations aim to reproduce the non linear behaviour of the digging depth as a function of the temperature and to measure the ability of the droplet to cool down the granular material. The numerical experiment is based on the same material properties as the physical experiment, these properties are summarised in Table 2. Fig. 8 illustrates the experimental setup and the numerical domain. The mesh size close to the droplet is refined to capture the droplet motion and the fluidisation of the granular medium. Further away from the droplet, the mesh size is increased to reduce the computational cost. Appendix A provides details on void fraction computation and force integration.

The Section 1 describes the model used to track the digging droplet in vaporisation. As the numerical model lives in a two-dimensional domain, the numerical considerations employed to mimic the experiment are then presented. In the following section, the droplet is followed for different granular bed temperatures to highlight the different regimes. The heat exchange governing the digging is then investigated in this regime at a initial temperature of 400 °C, as seen in Fig. 9. Finally, similarities and differences between the experiment and the numerical results are provided.

4.1. Droplet representation

As the droplet falls through the granular bed, it begins to absorb grains. The particles and the surrounding fluid contribute to the dynamics of the droplet and to its vaporisation. The droplet is modelled as a mixture of liquid phase and particles. The shape of a droplet is determined by the balance between buoyancy and surface tension, as well as the balance between inertial and viscous forces. These two balances are modelled respectively by the Eötvös number Eo and the Reynolds number Re_D. An approximation of the shape of the droplet can be obtained using the Grace diagram [41]. In the experiment, these numbers are given by

$$\mathrm{Eo} = \frac{\Delta \rho g D^2}{\sigma} \approx 1, \quad \mathrm{Re}_D = \frac{\rho D U}{\eta} \approx 10.$$

The droplet is then assumed to retain its shape and only its mass and radius are modified. This hypothesis is also supported by the experimental observation from Lin [2]. During the droplet digging, its shape stays circular until the droplet reaches its maximal depth. At this point, the droplet does not have enough energy to fluidise and the digging stops, the droplet fills up with grains. A spherical cohesive structure can be extracted from the digging which tends to confirm that the droplet shape is almost constant and does not dominate the digging process. The volume of the droplet V is given by the volume occupied by the liquid phase V_f and the absorbed particles V_p. The heat flux at the interface is entirely used to vaporise the water. The mass ratio $\dot{m}$ is then given by the latent heat of vaporisation $\mathcal{L}$ and the net heat flux. This heat flux is the sum of the transfer between the droplet and the surrounding air, Q_f and the transfer from the particles immersed in the droplet Q_p. The droplet dynamics is derived from the Volume-Averaged Navier–Stokes equations, Eq. (2), integrated over the droplet volume. The stress tensor is computed using the solution in the fluid phase since the inside of the droplet is not solved. The droplet is then fully described by the following equations,

$$V = V_f + V_p \tag{15}$$

$$\mathcal{L}\dot{m} = Q_f + Q_p \tag{16}$$

$$m\frac{\mathrm{d}\boldsymbol{u}}{\mathrm{d}t} = \boldsymbol{F}_f + \boldsymbol{F}_p + m\boldsymbol{g}, \tag{17}$$

where $\boldsymbol{F}_f$ is the force applied by the fluid on the particles and $\boldsymbol{F}_p$ is the force applied by the particles on the fluid. It is worth noting that the resulting surface tension over the boundary is null as the droplet remains circular. Fig. 10 illustrates the heat, mass and momentum transfer over the droplet.

4.2. Numerical considerations

To represent the initial conditions of the experiment, the granular bed is represented as an assembly of discs. A space-filling algorithm is used to minimise voids between particles [42]. As solid packing fraction controls the fluidisation of a granular bed, particles are assumed to be porous to maintain a volume fraction similar to the physical experiment measured at $\phi \approx 0.4$.

In order to limit the granular medium's ability to reorganise itself, cohesion is added between the grains. The vapour field ψ acts as an indicator of the fluidisation of the granular medium. A contact is considered cohesive if it persists for several time steps and it is not located in a fluidised region [43]:

$$F_c = \begin{cases} F_c^0 & \text{if } \psi < \psi^0, \\ 0 & \text{otherwise} \end{cases} \tag{18}$$

where ψ is the vapour concentration at the contact point and ψ^0 the vapour threshold. This is equivalent to assuming negligible the capillary force in the pendular regime and a constant force in the funicular regime.

The vapour field is described by the advection-diffusion equation;

$$\epsilon \rho_v \frac{\mathrm{d}\psi}{\mathrm{d}t} = \boldsymbol{\nabla} \cdot \left(\epsilon D_v \boldsymbol{\nabla} \psi \right) \tag{19}$$

where ρ_v is the vapour density and D_v is the vapour diffusion coefficient. The cohesive force is modelled by a contact force between the grains integrated into the non-smooth contact dynamics.

Since the walls are used to heat the granular medium, they are assumed to maintain a constant temperature $\hat{T}_p$, which corresponds to the initial temperature of the grains. The high temperature of the granular bed rapidly heats the droplet to its vaporisation temperature $\hat{T}_d = 100$ °C. This transient heating process is considered instantaneous, after which the droplet is assumed to be at its vaporisation temperature. The produced vapour generates a flow from the droplet to the surrounding fluid in the radial direction, denoted $\hat{\boldsymbol{r}}$. At the top of the domain,
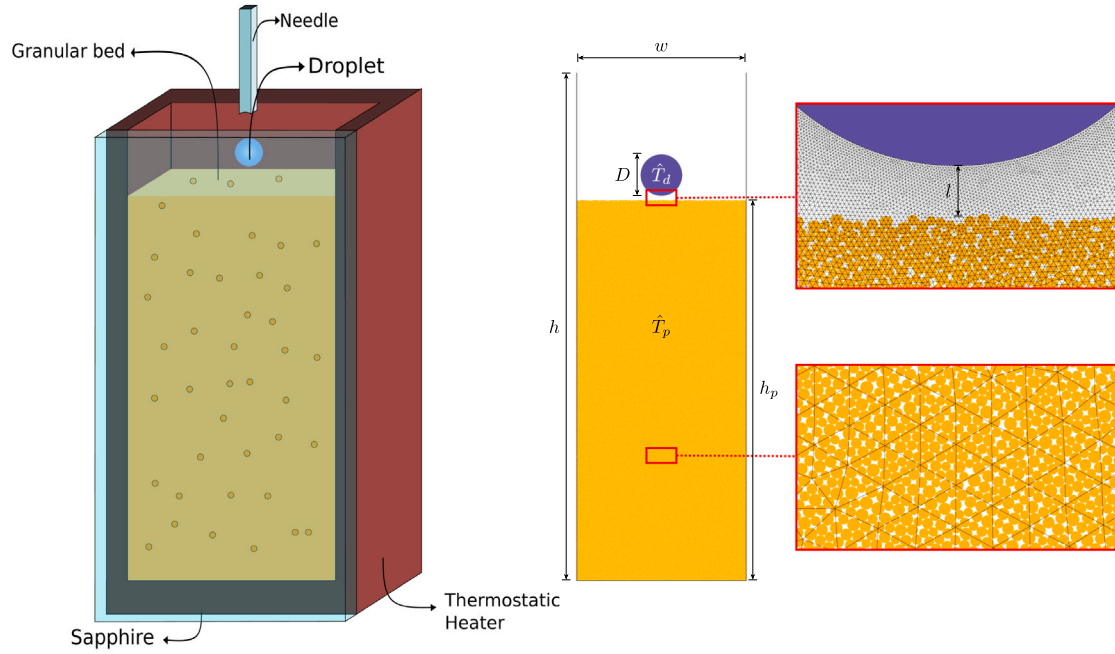
Fig. 8. On the left, schematic of the experiment. On the right, its numerical representation. The mesh close to the droplet is refined and the mesh further away is larger than the particle size.

Table 2
Properties associated to the spontaneous digging experiment.

Fluid properties			Grain properties		
Density, ρ	kg m^{-3}	1.204	Density, ρ	kg m^{-3}	3200
Viscosity, η	kg m^{-1} s^{-1}	2 10^{-5}	Heat capacity, c	J kg^{-1} K^{-1}	290
Heat capacity, c	J kg^{-1} K^{-1}	1040	Heat conductivity, k	J s^{-1} m^{-1} K^{-1}	234
Heat conductivity, k	J s^{-1} m^{-1} K^{-1}	0.026	Young's modulus, E	kg m s^{-1}	10^{11}
Thermal expansion, β	K^{-1}	3 10^{-3}	Poisson's ratio, ν	\	0.35
Vapour diffusivity, D_v	m^2 s^{-1}	2 10^{-5}	Dry friction, μ	\	0.3
Vapour density, ρ_v	kg m^{-3}	1.204			
Geometry properties			Numerical parameters		
Width, w	mm	10	Time step, Δt	s	5 10^{-4}
Height, h	mm	30	Cohesive bond, F_c^0	kg m s^{-2}	7.5 10^{-4}
Bed height, h_p	mm	22.5	Vapour threshold, ψ^0	\	0.9
Droplet height, l	mm	1.5			
Droplet diameter, D	mm	2.5			
Grain diameter, d	μm	55			

an outflow boundary condition is applied. The boundary conditions applied to the fluid conservation equations and the vapour field can be summarised as,

Outflow	Wall	Droplet
$f = n \cdot (\sigma - \epsilon \rho u u)$	$u = 0$	$u = u_d + \frac{\dot{m}}{\rho_v S} \hat{r}$
$q = n \cdot (-q - \rho c u T)$	$T = \hat{T}_p$	$T = \hat{T}_d$
$\psi = n \cdot (\epsilon D_v \nabla \psi - \rho_v u \psi)$	$\psi = 0$	$\psi = 1$

These boundary conditions are used to mimic the experimental setup. Depending of the heating device and on the border mass, the characteristic time to heat the granular assembly at the requested temperature is much longer that the digging process that lasts about one minute. The temperature of the granular material changes at the vicinity of the droplet. However, since the droplets are far from the border, except in the depth direction, the wall temperature can be considered as constant. The front and rear walls are made of sapphire or aluminium, respectively. Three facts can be evidenced to claim for constant temperature walls: first, the droplet digs, that means that the

droplet moves and does not cool down the wall at the same place. Second, the walls are made of high thermal conductivity materials compared to the granular material. Third, the mass of the walls are large compared to the droplet. We can consider that the walls are thermal reservoirs.

The numerical scheme is summarised in Fig. 11. At each time step, the local fluid volume fraction over the domain is computed. To couple the fluid conservation equations with particles, a semi-implicit scheme is used [25]. Energy equation is solved to compute the temperature field based on Eq. (3) using the Nusselt correlation (13). Mass rate is computed based on the heat flux at the droplet interface using Eq. (16). It provides the boundary condition to close the fluid model at the droplet interface. Momentum conservation is solved using Eq. (2) with the momentum transfer between the fluid and the particles (12). The force from the fluid and the particles are exerted on the droplet to compute its motion, based on Eq. (17). The droplet volume is updated based on the mass rate and the particles entering the droplet (15). Once the droplet has been updated, the mesh is deformed to track the droplet motion. To keep the mesh quality, mesh nodes close to the droplet are moved radially while keeping conformity with the droplet boundary. A
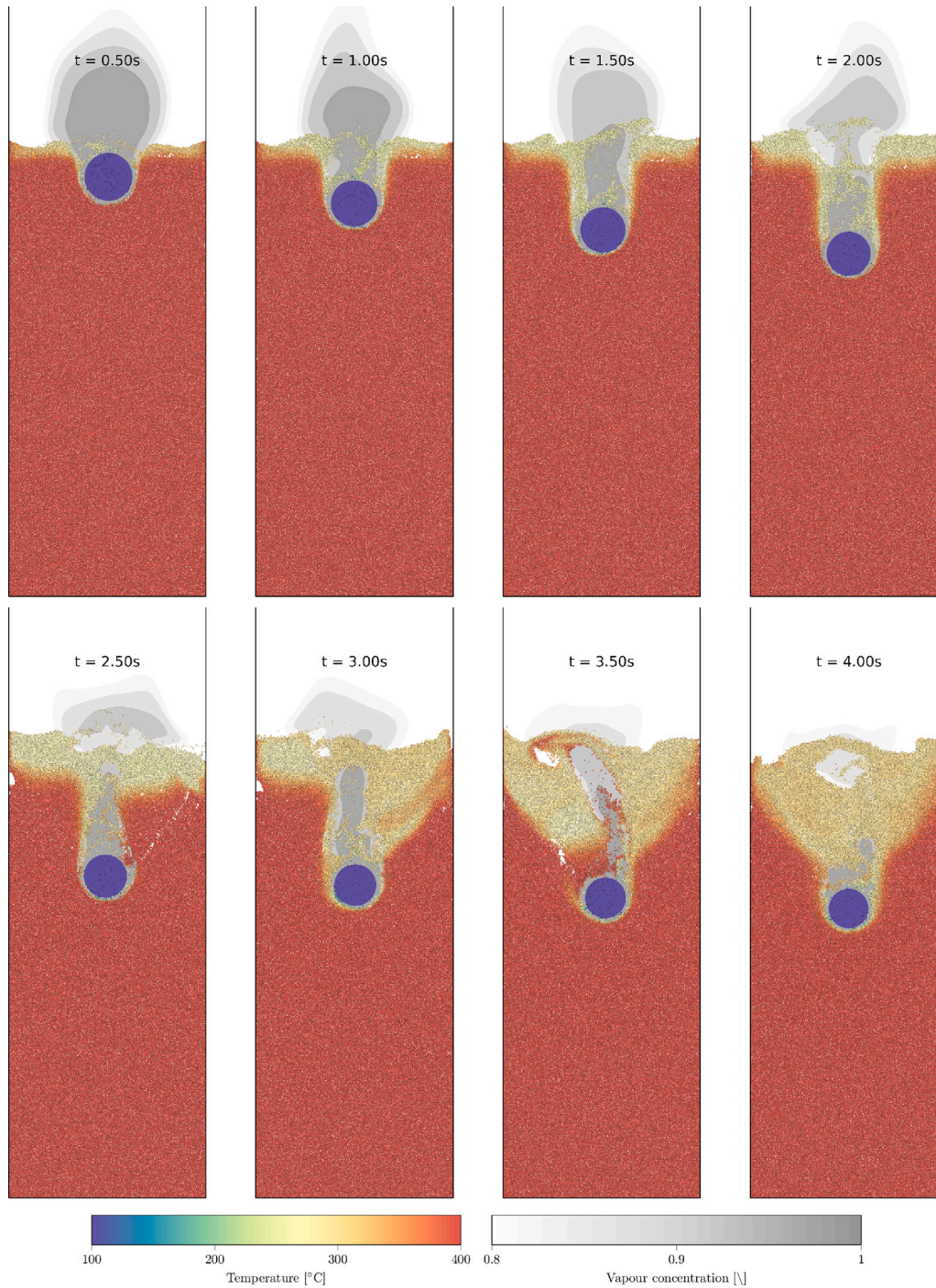
Fig. 9. Snapshots of the droplet penetrating the granular bed at 400 °C. The vapour field is indicated by shades of grey. The temperature of the grains is shown in red. The grains are ejected into the chimney as the droplet falls. The fluidisation of the grains allows the droplet to continue falling. (For interpretation of the references to colour in this figure legend, the reader is referred to the web version of this article.)

node will be moved by the following expression:

$$
x_{new} = \begin{cases} x - \left(1 - \frac{\|x - x_d\| - r_d}{L}\right) u_d \Delta t, & \text{if } \|x - x_d\| < r_d + L \\ x, & \text{otherwise} \end{cases} \tag{20}
$$

where x is the node position, x_d is the droplet position, r_d is the droplet radius, L is the maximal from where a node can move, its value has been set to $L = 1.5 r_d$, and u_d is the droplet velocity. The node velocity is taken into account in the material derivative in the conservation equations using the Arbitrary Lagrangian-Eulerian (ALE) framework,

$$
\frac{d\bullet}{dt} = \frac{\partial\bullet}{\partial t} + (u - u_m) \cdot \nabla\bullet \tag{21}
$$

where u is the fluid velocity, u_m is the mesh velocity. The mesh velocity is integrated explicitly in the time integration scheme, which leads to a non-conservative ALE method. To avoid mesh distortion, the domain is remeshed every 25 time steps, equivalent to every 0.0125 s. GMSH has been used as the mesh generator. At this rate, remeshing has no impact on the computational cost which is dominated by the contact dynamics and the linear system resolution. Once the domain has been remeshed, all the fluid degree of freedom are interpolated from the previous mesh to the new one.
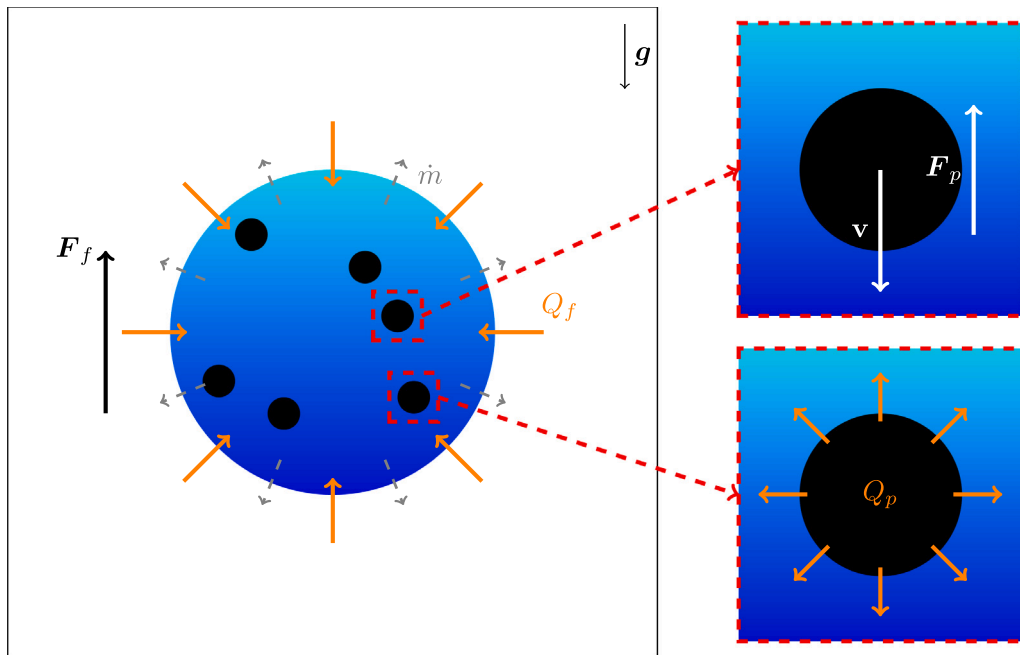
Fig. 10. Droplet representation. The motion of the droplet is balanced by its weight mg, the force exerted by the particles F_p and the force exerted by the surrounding fluid F_f. Due to the temperature gradient, the droplet is subject to a heat flux Q_f from the surrounding fluid and a heat flux Q_p from the particles. The net heat transfer is used to vaporise the droplet.

4.3. One droplet, three regimes

As briefly detailed above, when the droplet falls into the granular medium, three regimes are obtained depending on the initial temperature of the granular bed. These three regimes are characterised by the ability of the droplet to fluidise the granular medium: (i) at low temperatures, the droplet cannot fluidise on a long time, (ii) at intermediate temperatures, the droplet digs, and (iii) at high temperatures, the droplet remains at the top layers of the granular bed.

Fig. 12 illustrates the final depth reached by the droplet for different temperatures ranging between 300 and 600 °C. Three regimes are found. In the first regime, for temperatures below 350 °C, the droplet crashes into the granular medium without being able to fluidise its surrounding environment. The depth of the droplet is then limited to the depth of the initial cavity, and the droplet does not hollow out. Consequently, the droplet vapourizes at the surface of the granular bed without ejections. On the other hand, at the highest temperatures, one expects a large and violent ejection of grains since the production of vapour increases with the temperature of the bed. However, we observe that below the droplet, the grains are ejected but because the vapour gap is large, the grains reorganise below the droplet before the droplet can take their place. The intermediate regime is observed for temperatures between 350 and 500 °C. In this regime, vapour ejection is sufficient to locally fluidise the granular medium without stopping the droplet from falling. Indeed, the grains below the droplet do not have time to reorganise before the droplet takes their place.

Regarding the change of temperature produced by the passage of the droplet, in Fig. 12, the colour of the grains is related to their temperature (see colour bar). The area cooled down by the droplet can therefore be observed. Remarkably, even if the droplet does not dig deep, the temperature is modified on a range equivalent to at least one droplet diameter, see $T = 500$ °C for example.

The droplet depth evolution, namely the depth h reached by the droplet normalised by its diameter as a function of dimensionless time, is shown in Fig. 13 and this, for four initial temperatures of the bed. Dimensionless time is defined as the free fall time for the droplet to travel its radius. We observe the same behaviour during the first second. The droplet manages to penetrate the first layers of grains

with the same apparent speed. Then, according to the temperature, the droplet speed decreases before stopping at the maximum depth that depends on the considered temperature. Note the peculiar behaviours at 500 and 600 °C for which the droplet bounces back upwards. This is due to the reorganisation of the grains below the droplet. The vapour gap is large enough to allow the vapour to escape without entraining grains. The grains move and reorganise provoking the local collapse of the chimney. The droplet then goes up. On the other hand, when the droplet digs, it can reach depths 10 times its initial radius. The maximum depth is reached at a temperature of 400 °C.

Fig. 14 illustrates the evolution of the dimensionless falling velocity with respect to dimensionless time for the same four temperatures of Fig. 13. As observed on the trajectories, the starting speeds are of the same order of magnitude whatever the temperature of the granular bed. The speed of fall decreases as a function of time as the impact of vaporisation becomes more and more important as the droplet loses mass. The third regime is characterised by temperatures above 500 °C. In this case, the droplet is considerably slowed down by the ejection of steam, even though the grains are highly fluidised. The droplet starts to bounce onto the granular bed and rises back to the surface.

The dependence of the speed with the temperature is not monotonous. If we measure the speed at $t = 2$ s, the speed increases with the temperature until $T = 400$ °C before decreasing. The speed for the first and third regime is roughly zero as the droplet cannot dig. The maximal speed and depth is found for the intermediate temperature, namely when $T = 400$ °C.

Comparing the simulations to the experiments, we can see that the major features are fully reproduced by the simulations: (i) The three regimes are found, two non-digging and one digging regime, (ii) The depth is found to increase with time before stopping at a given depth that depends on the temperature, (iii) the digging speed is maximum at an intermediate temperature, and (iv) the reached depths depend on the temperature and a maximum of the digging depth is found when T = 400 °C. This is what is observed in the quasi-2D experiments. The bounce back of the droplet is however not observed in the experiments. Another difference with the experiments is that the droplet takes some time to cross the interface before showing the constant digging speed regimes. This difference with the simulations is attributed to the large
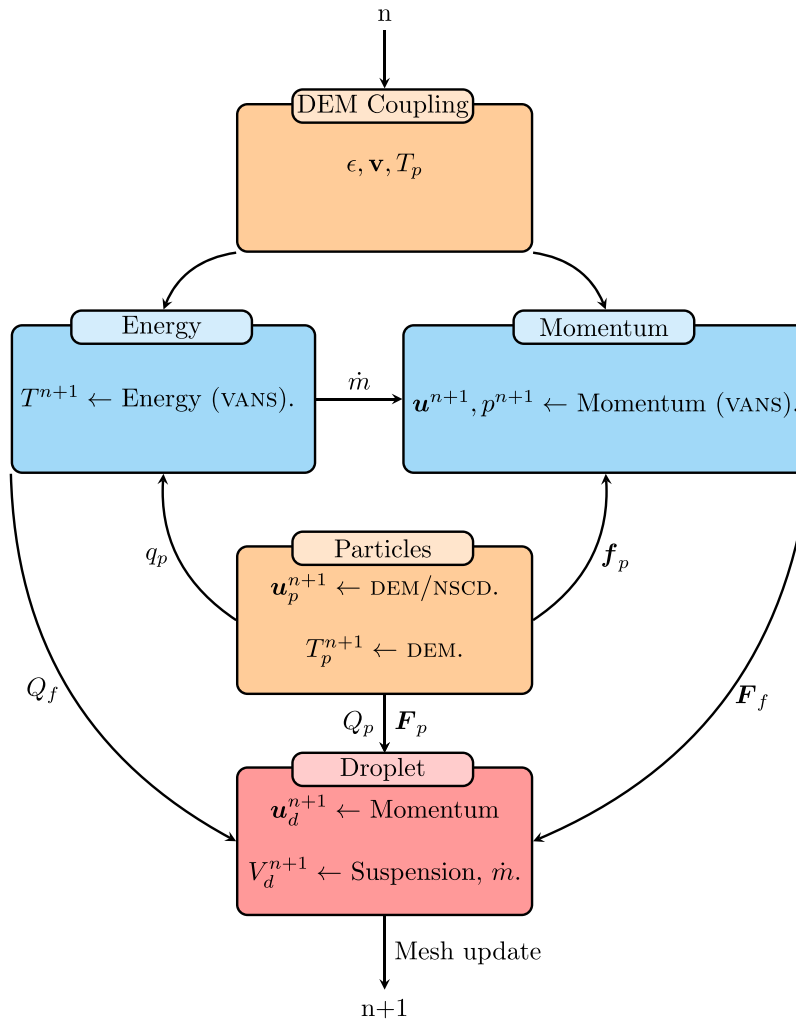
n

$$\boxed{\text{DEM Coupling}}$$

$$\epsilon, \mathbf{v}, T_p$$

$$\boxed{\text{Energy}}$$

$$T^{n+1} \leftarrow \text{Energy (VANS).}$$

$$\dot{m}$$

$$\boxed{\text{Momentum}}$$

$$\boldsymbol{u}^{n+1}, p^{n+1} \leftarrow \text{Momentum (VANS).}$$

$$q_p$$

$$\boldsymbol{f}_p$$

$$\boxed{\text{Particles}}$$

$$\boldsymbol{u}_p^{n+1} \leftarrow \text{DEM/NSCD.}$$

$$T_p^{n+1} \leftarrow \text{DEM.}$$

$$Q_f$$

$$\boldsymbol{F}_f$$

$$Q_p \quad \boldsymbol{F}_p$$

$$\boxed{\text{Droplet}}$$

$$\boldsymbol{u}_d^{n+1} \leftarrow \text{Momentum}$$

$$V_d^{n+1} \leftarrow \text{Suspension, } \dot{m}.$$

Mesh update

n+1

Fig. 11. Numerical procedure.

thermal gradients that are found along the first layers of grains in the experiments. This is due to radiation and heat exchange with the atmosphere that decrease the temperature of the first layers compared to the bulk. This explains the difference with the numerical simulations for which the temperature of the grains is more homogeneous. As a consequence, the droplet experiences some difficulties to cross the interface in the experiments.

In the experiments, as soon as the droplet is at a depth larger than its diameter, the droplet digs with a constant speed. That is less marked in the numerical simulations. Indeed, the difference is probably due to the fact that the simulations are pure 2D and to the fact that experiments are quasi-2D. The ejection of the grains is not eased by the 2D constraints since the grains organise along very compact configurations. Finally, we cannot reject the influence of the border in the experimental set-up: the front side is made of sapphire and the rear side of copper. This friction is consequently not capture in the model.

As suggested by Fig. 12, fluidisation of the granular medium promotes heat transfer between the droplet and the granular medium. This increase can be seen in the average temperature of granular bed over time, which can be observed in Fig. 15. The temperature was normalised in order to be compared with the four considered starting temperature. At 400 °C, the temperature decreases is the most efficient because the droplet goes the deepest interacting with more grains. Generally speaking, in the intermediate temperatures, the droplet motion is characterised by a prolonged period of fluidisation, increasing the cooling of the grains. In addition, the ejection of grains

into the chimney allows the droplet to cool grains that are initially deeper and still hot. The third regime does not follow this behaviour. Indeed, the reorganisation of the granular medium before the droplet falls leads to weaker interaction between the droplet and the granular medium because the temperature differences are smaller. The heat transfer is localised at the first layers of the granular material, the heat being conveyed to the droplet thanks to the contact network between the grains. In all regimes, a screening effect is observed as the droplet becomes saturated with grains. Heat is then transferred less effectively between the droplet and the granular medium. This effect is particularly visible in Fig. 16 indicating an estimate of the instant lifetime of the droplet over time.

The instant lifetime is calculated as $m(t)/\dot{m}(t)$ and reported in Fig. 16. This quantity allows to track the effective heat transfer as a function of time. In the initial stages of the fall, the grains passing through the droplet are rapidly ejected into the chimney and do not produce any screening effect. The lifetime is then of the order of ten seconds. Subsequently, the droplet becomes saturated with grains, the medium containing the droplet is then described as a wet medium and the heat is transferred less effectively. The lifetime increases sharply, reaching up to several minutes. The heat transfer is observed to be maximum at $T = 400$ °C which is coherent with the previous observations. As soon as the droplet sits and does not move, the heat transfer decreases and a plateau is observed. The heat transfer can then only proceed along the contact network and along the exchange with the gas. This contrasts with the moving droplet whose environment is at a larger temperature.
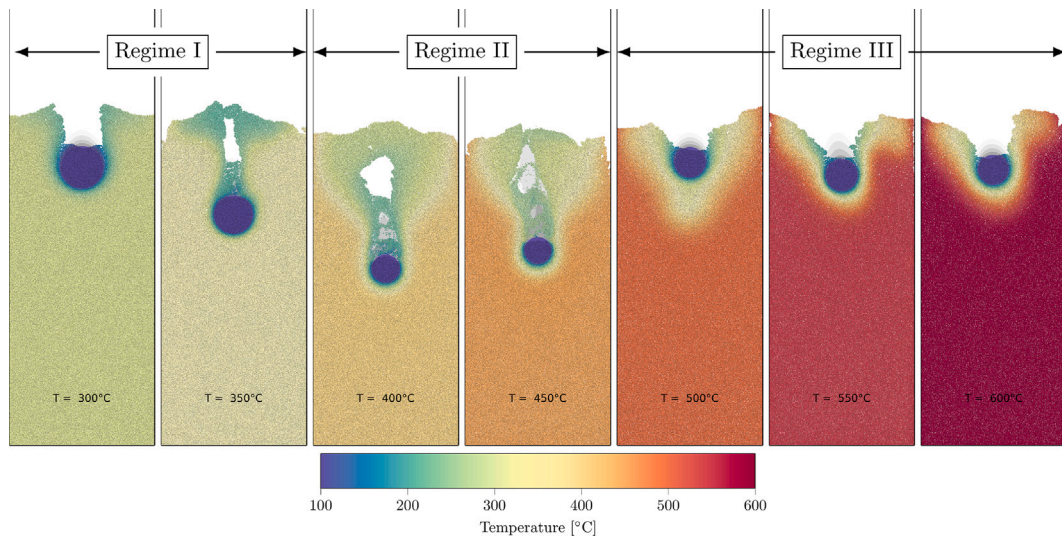
Fig. 12. Final depth reached by the droplet at different initial temperature of the granular bed. (For interpretation of the references to colour in this figure legend, the reader is referred to the web version of this article.)
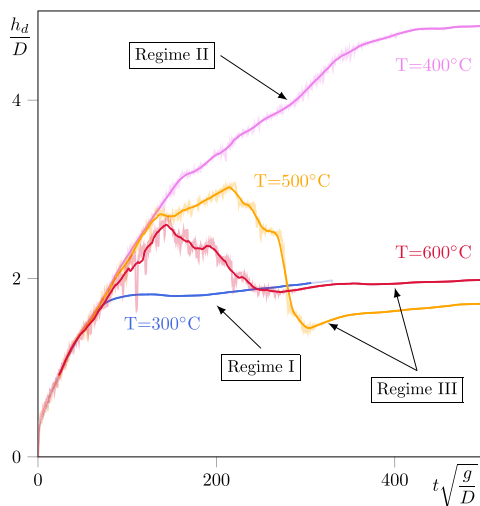

Fig. 13. Droplet depth evolution. Depth is made dimensionless using the initial droplet diameter as a characteristic length. Using this length and the gravitational acceleration, the characteristic time is build to make the evolution time dimensionless.
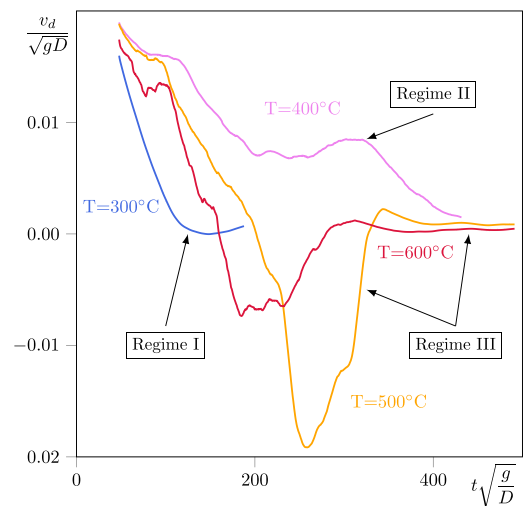

Fig. 14. Droplet vertical velocity evolution Characteristic droplet velocity and the droplet diameter are used to define the dimensionless falling velocity and the dimensionless time.

4.4. Spontaneous digging at 400 °C

Since transfer is maximal at a temperature of 400 °C, the droplet was carefully monitored at this temperature. Fig. 9 shows the droplet penetration into the granular bed at different snapshots for a granular bed temperature of 400 °C at 8 different times (see Legend). The chimney starts building already after the first seconds. The cone of cooling is clearly visible at $t = 3$ s and even some bubbles of vapour can be seen.

As the droplet interacts with the granular medium, a thick layer of vapour is produced. The droplet is strongly slowed down by the force of the steam and this ejection allows the grains to be fluidised around the droplet. Finally, the grains are ejected in the wake of the droplet, and the droplet is able to take the place of the ejected grains and continues to dig. The different forces acting on the droplet can be isolated and measured as a function of time. The weight mg, the fluid–particle force F_f, the particle–fluid force F_p, and the resulting force F_{net} are presented as a function of time in Fig. 17. In parallel, one can also follow the evolution of the heat exchange Q_p, Q_f and Q_{net} in Fig. 18. The forces

have been scaled by the initial weight of the droplet and the heat fluxes by the initial conductive flux at the droplet interface.

When the droplet fully penetrates the granular medium, the average forces applied by the vapour and the grains balance the weight of the droplet. The droplet then reaches its terminal velocity. Particles ejected in the wake of the fall form a chimney which is maintained by the fluidisation of the grains. As the droplet falls, the particles ejected into the chimney fall back down and pass through the droplet, cooling the granular medium. This leads to a reduction in heat flow in close proximity to the droplet as seen in Fig. 18. Fluidisation of the granular medium is then reduce. Once fluidisation stops, the droplet absorbs the grains through its front. The droplet is then slowed down by the captured grains, and the thrust force of the vapour is insufficient to keep the droplet levitating. Digging stops and the droplet comes to rest.

As the droplet falls, it only cools the grains in its wake. The deeper the droplet, the longer the chimney and the grains within it are cooled. The temperature under the droplet changes only slightly during the fall. Fig. 19 shows the vertical average particle temperature profile. Grains in the chimney are cooled by the droplet without reaching
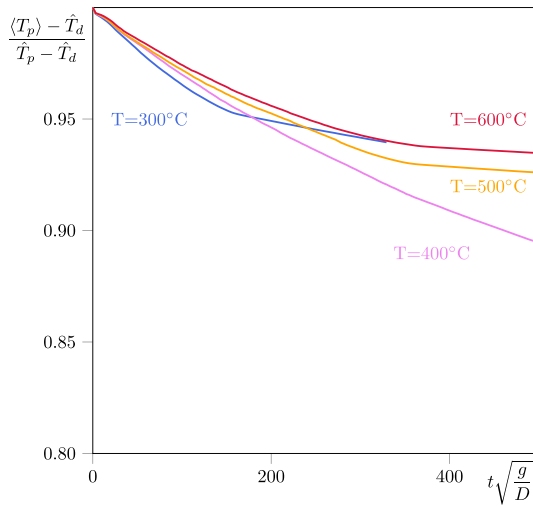
Fig. 15. Mean particle temperature evolution. The dimensionless temperature measures the particle temperature relative to its initial difference with the droplet. The characteristic time is obtained by considering a free-fall of the droplet using its diameter as the characteristic length.
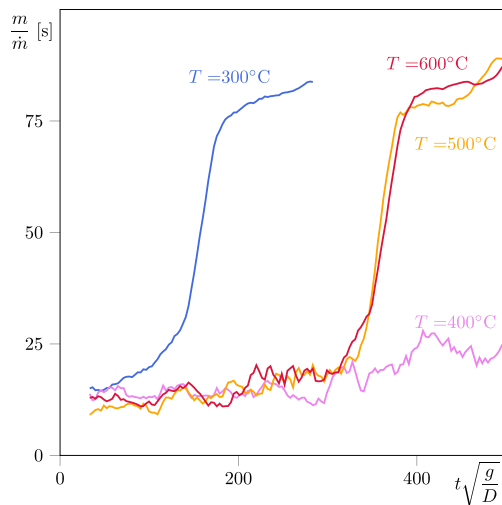

Fig. 16. Droplet instantaneous lifetime, which is estimated as the time required for the droplet to evaporates its mass based on the instantaneous vaporisation rate. The time scale is made dimensionless using the time taken for the droplet to fall of its radius in a free-fall situation.

Fig. 17. Force contribution evolution to the droplet motion.

Fig. 18. Heat transfer evolution over the droplet.

the vaporisation temperature. As the droplet gathers grains in itself, they reach vaporisation temperature. Then, they are ejected into the chimney where their temperature increases. The resulting temperatures reach half their initial temperature. This effect can be seen in Fig. 20 which shows the horizontal average particle temperature profile at a specific height.

5. Conclusion

This paper presents a multiphysics model that describes the flow of grains in a fluid including heat transfer. To accurately represent this flow, a volume averaged stabilised finite element method has been coupled with a non-smooth discrete element method. Particular emphasis is placed on modelling the heat exchange between the grains and the fluid. The averaged fluid description requires the introduction of constitutive laws to represent the transfer of momentum and heat between the grains and the fluid. A correlation equation, Eq. (13), for grain assemblies has been introduced to quantify heat transfer, based
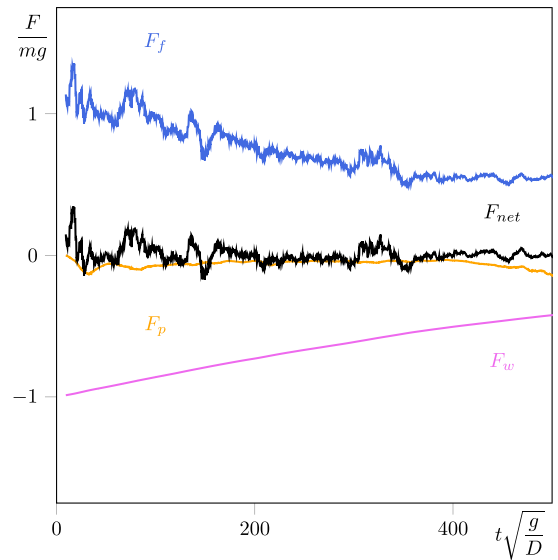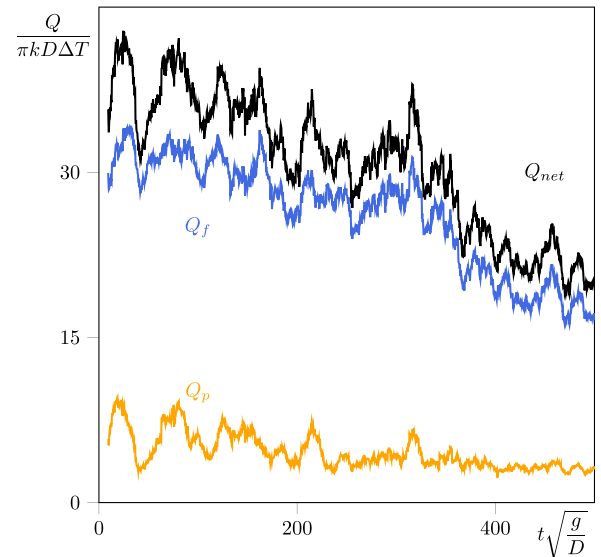
on the Reynolds analogy [30] and the Di Felice pore function [31]. The proposed law was validated against experimental measurements of heated granular beds taken from the literature [20]. The implementation of the model was then validated on the study of a bubbling fluidised granular bed by reproducing Patil's experiment [21].

The two-dimensional model was then applied to the study of the spontaneous digging of a droplet of water in a hot granular bed. Depending on the temperature, the vaporisation of the droplet causes the granular bed to fluidise locally and dig into the granular bed. The absorption of grains within the droplet is achieved by representing the droplet as a mixture of water and grains.

Depending on the temperature of the granular bed, three regimes were observed as expected from the experiment. The first regime is characterised by no digging, the vaporisation of the water is not sufficient to fluidise the granular bed and the water droplet remains on the surface. The second regime, obtained at intermediate temperatures, is characterised by deeper digging. The water vaporisation is sufficient to fluidise the granular bed while allowing the droplet to fall. The
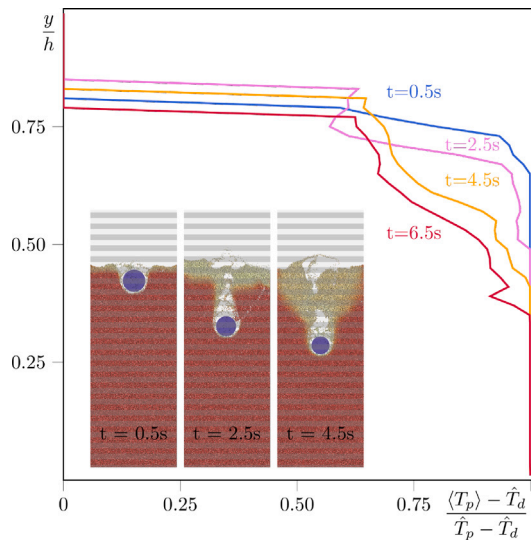
Fig. 19. Vertical particle temperature profile at different snapshots. The alternating greys cells indicates the cell decomposition on which the averaging process is performed.
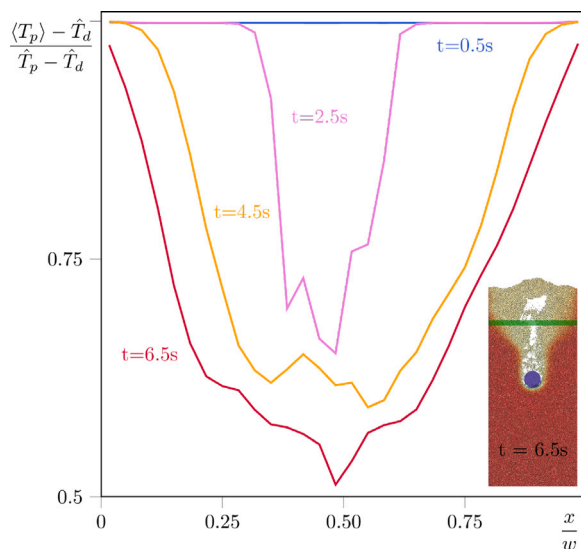

Fig. 20. Horizontal particle temperature profile in a given cell highlighted in green. (For interpretation of the references to colour in this figure legend, the reader is referred to the web version of this article.)

droplet takes the place of the grains and penetrates into the granular bed. At high temperatures, the third regime is reached where the droplet returns to the surface. Vaporisation slows the droplet's fall, allowing the granular bed to reorganise around the droplet, preventing it from sinking. The model greatly simplifies the experiment as the local fluidisation of a granular bed is controlled by the cohesion of the grains. This parameter has a significant effect as it limits the mobility of the grains, which can favour digging by preventing the grains from reorganising around the droplet. However, the numerical model reproduces the main trends of the experiment, namely digging, local fluidisation and chimney formation. The bidimensional numerical experiment simplifies the three-dimensional experiment. However, as grains are constrained to move in the plane, given the same force, it is more difficult to fluidise the bi-dimensional granular bed than the three-dimensional one. This is why the droplet is able to dig at higher

temperatures as more energy is needed to fluidise the bed. Moreover, the range of temperatures for which the droplet digs is narrower in the two-dimensional case than in the three-dimensional case.

The vaporisation of the droplet is the main source of heat transfer in the system and enables a local fluidisation in the wake of the fall. When the grains are absorbed by the droplet, a screening effect is observed which reduces the heat transfer. However, the heat contributed by the retained grains does not account for the majority of the heat exchanged with the fluid. The fluid remains hot through the granular bed. Evaporation reduces the surface area of the droplet, thereby reducing vaporisation. When the vaporisation is no longer sufficient to eject the grains towards the chimney, the droplet stops falling. It then fills up with grains at the front and stops. The droplet becomes saturated and can no longer transfer heat to the outside. Its lifetime then increases considerably.

Future work will include investigating the effect of cohesion and the effect of grain size on digging time. Grain size controls the fluidisation of the granular bed as smaller grain systems can be more easily disrupted by fluid injection. This future work will provide a better understanding of the phenomenon of spontaneous digging and enable us to control it more effectively. The effect of droplet shape on digging will also be investigated as the droplet tends to deform to minimise its surface energy. This deformation can affect the digging during the crossing of the granular interface. Extending the model to three dimensions is a natural step in studying the phenomenon of digging, which reduces the geometric constraints of the assembly.

CRediT authorship contribution statement

Michel Henry: Writing – review & editing, Writing – original draft, Visualization, Validation, Software, Project administration, Methodology, Investigation, Formal analysis, Data curation, Conceptualization. **Nathan Coppin:** Writing – review & editing, Writing – original draft, Visualization, Software, Resources. **Stéphane Dorbolo:** Writing – review & editing, Writing – original draft, Visualization, Validation, Supervision, Methodology, Investigation, Formal analysis, Data curation, Conceptualization. **Vincent Legat:** Writing – review & editing, Writing – original draft, Visualization, Supervision, Resources, Project administration, Funding acquisition, Data curation, Conceptualization. **Jonathan Lambrechts:** Writing – review & editing, Writing – original draft, Supervision, Software, Project administration, Methodology, Investigation, Data curation, Conceptualization.

Declaration of competing interest

The authors declare that they have no known competing financial interests or personal relationships that could have appeared to influence the work reported in this paper.

Acknowledgements

Appendix A. Spatial discretisation

In this appendix, the discretised weak form of the volume averaged Navier–Stokes equations is presented within the finite element method framework. Then, the smooth grain representation used for the fluid is detailed, *i.e.* the void fraction and the solid velocity computations.

Discretised weak form

The volume averaged Navier–Stokes equations are discretised using the finite element method on an unstructured grid. The test solution spaces for the velocity, pressure and temperature are respectively denoted by $\mathcal{U}^h$, $\mathcal{P}^h$ and $\mathcal{T}^h$.

$$\boldsymbol{u} \approx \boldsymbol{u}^h = \sum_{i}^{n} \boldsymbol{U}_i \phi_i, \qquad \boldsymbol{u}^h \in \mathcal{U}^h \tag{A.1}$$

$$p \approx p^h = \sum_{i}^{n} \boldsymbol{P}_i \phi_i, \qquad p^h \in \mathcal{P}^h \tag{A.2}$$

$$T \approx T^h = \sum_{i}^{n} \boldsymbol{T}_i \phi_i, \qquad T^h \in \mathcal{T}^h \tag{A.3}$$

where n refers to the number of nodes as linear equal-order interpolation functions are used for all the fields. This choice is motivated to keep the numerical efficiency of the multiscale model. However, the Brezzi-Babuska condition is not satisfied and the discretisation leads to a singular discrete matrix. In order to restore the rank deficiency, a pressure stabilisation/Petrov–Galerkin (PSPG) term is added to the continuity equation.

The continuous Galerkin method can also leads to difficulty when applied to a convective dominated problem as the convection term is not symmetric positive definite. Therefore, the best approximation property is not satisfied and the solution may be oscillatory. In order to limit this effect, the test functions are enriched with a streamline upwind Petrov–Galerkin (SUPG) term. This term is added to the momentum equation and the energy conservation. It is equivalent to adding a numerical diffusivity in the flow direction.

These stabilisations have a major drawback, once they become dominant, the accuracy of the solution is not guaranteed. Therefore, the stabilisation parameters have to be carefully chosen. In the case of the PSPG, the loss of incompressibility should be limited. To restrict this effect, the least square incompressibility constraint is used. It is convenient to describe these stabilisations as residue-based stabilisation methods where

$$R_p = \frac{\partial \epsilon}{\partial t} + \boldsymbol{\nabla} \cdot (\epsilon \boldsymbol{u}) \tag{A.4}$$

$$\boldsymbol{R}_u = \epsilon \rho \, \frac{\mathrm{d}\boldsymbol{u}}{\mathrm{d}t} - \boldsymbol{\nabla} \cdot \boldsymbol{\sigma} - \boldsymbol{f}_p + \left(1 + \beta \left(T - T_R \right) \right) \epsilon \rho \boldsymbol{g} \tag{A.5}$$

$$R_T = \epsilon \rho c \frac{\mathrm{d}T}{\mathrm{d}t} + \boldsymbol{\nabla} \cdot \boldsymbol{q} - q_p \tag{A.6}$$

are the residue of the conservation equations.

The stabilised finite element formulation of the volume averaged Navier–Stokes equations is to find $(\boldsymbol{u}^h, p^h, T^h) \in (\mathcal{U}^h \times \mathcal{P}^h \times \mathcal{T}^h)$ such that $\forall (\hat{\boldsymbol{u}}^h, \hat{p}^h, \hat{T}^h) \in (\hat{\mathcal{U}}^h \times \hat{\mathcal{P}}^h \times \hat{\mathcal{T}}^h)$

$$\begin{aligned}
&\left\langle \frac{\partial \epsilon}{\partial t}, \hat{p}^h \right\rangle - \left\langle \epsilon \boldsymbol{u}^h, \nabla \hat{p}^h \right\rangle \\
&\quad + \left\langle\!\left\langle \epsilon \boldsymbol{u}^h, \hat{p}^h \boldsymbol{n} \right\rangle\!\right\rangle \\
&= - \underbrace{\sum_e \xi_p \left\langle \boldsymbol{R}_u, \nabla \hat{p}^h \right\rangle_e}_{\text{PSPG}}
\end{aligned} \tag{A.7}$$

$$\begin{aligned}
&\left\langle \epsilon \rho \frac{\mathrm{d}\boldsymbol{u}^h}{\mathrm{d}t} + \boldsymbol{\nabla} p^h - \left(1 + \beta \left(T - T_R \right) \right) \epsilon \rho \boldsymbol{g} - \boldsymbol{f}_p, \hat{\boldsymbol{u}}^h \right\rangle \\
&\quad + \left\langle \epsilon \eta \left(\boldsymbol{\nabla} \boldsymbol{u}^h + \boldsymbol{u}^h \boldsymbol{\nabla} \right), \nabla \hat{\boldsymbol{u}}^h \right\rangle \\
&\quad - \left\langle\!\left\langle \epsilon \eta \left(\boldsymbol{\nabla} \boldsymbol{u}^h + \boldsymbol{u}^h \boldsymbol{\nabla} \right), \hat{\boldsymbol{u}}^h \cdot \boldsymbol{n} \right\rangle\!\right\rangle \\
&= - \underbrace{\sum_e \xi_u \left\langle \boldsymbol{R}_u, \boldsymbol{u}^h \cdot \nabla \hat{\boldsymbol{u}}^h \right\rangle_e}_{\text{SUPG}} - \underbrace{\sum_e \xi_c \left\langle R_p, \nabla \cdot \hat{\boldsymbol{u}}^h \right\rangle_e}_{\text{LSIC}}
\end{aligned} \tag{A.8}$$

$$\begin{aligned}
&\left\langle \epsilon \rho c \frac{\mathrm{d}T^h}{\mathrm{d}t} - q_p, \hat{T}^h \right\rangle + \left\langle \epsilon k \boldsymbol{\nabla} T^h, \nabla \hat{\boldsymbol{u}}^h \right\rangle \\
&\quad - \left\langle\!\left\langle \epsilon k \boldsymbol{\nabla} T, \hat{\boldsymbol{u}}^h \cdot \boldsymbol{n} \right\rangle\!\right\rangle \\
&= - \underbrace{\sum_e \xi_T \left\langle R_T, \boldsymbol{u}^h \cdot \boldsymbol{\nabla} \hat{T}^h \right\rangle_e}_{\text{SUPG}}
\end{aligned} \tag{A.9}$$

where $\langle \cdot, \cdot \rangle$ and $\langle\!\langle \cdot, \cdot \rangle\!\rangle$ represents the inner products on the domain Ω and its boundary $\partial\Omega$ for which the outer normal is denoted by $\boldsymbol{n}$. The restriction e indicates that the inner product is only performed on the interior of the element e. The stabilisation parameters are given by

$$\xi_c = h \, \|\boldsymbol{u}^h\| \min \left(\frac{h\rho\|\boldsymbol{u}^h\|}{6\eta}, \frac{1}{2} \right) \tag{A.10}$$

$$\xi_u = \xi_p = \left[\left(\frac{2}{\Delta t} \right)^2 + \left(\frac{\|\boldsymbol{u}^h\|}{h} \right)^2 + \left(\frac{4\eta}{\rho h^2} \right)^2 \right]^{-1/2} \tag{A.11}$$

$$\xi_T = \left[\left(\frac{2}{\Delta t} \right)^2 + \left(\frac{\|\boldsymbol{u}^h\|}{h} \right)^2 + \left(\frac{4k}{\rho c h^2} \right)^2 \right]^{-1/2} \tag{A.12}$$

where h is the element characteristic length. To estimate the rate of fluid volume fraction, the divergence of the mean solid velocity is used as both terms are related by the continuity equation,

$$\frac{\partial \epsilon}{\partial t} = \boldsymbol{\nabla} \cdot [\phi \boldsymbol{v}] \tag{A.13}$$

where ϕ is the volume fraction of the solid phase and $\boldsymbol{v}$ the solid velocity. By using the same semi-implicit scheme employed in the momentum conservation to predict the solid velocity, the model is able to compute the rate of porosity at low fluid volume fraction. Details on the discretisation of the solid velocity are given in the next section.

A smooth grains discretisation

The volume averaged Navier–Stokes equations assume the fluid volume fraction, *i.e.* the void fraction, to be continuous. However, the discrete representation of the grains is not continuous. To overcome this issue, the volume of each grains must be distributed over the mesh. The void fraction at the node i is then given by

$$\epsilon_i = 1 - \frac{\int_\Omega H_p(\boldsymbol{x}) \phi_i(\boldsymbol{x}) \mathrm{d}\boldsymbol{x}}{\int_\Omega \phi_i(\boldsymbol{x}) \mathrm{d}\boldsymbol{x}} \tag{A.14}$$

where $H_p(\boldsymbol{x})$ is the sum of the Heaviside functions associated to grains and $\phi_i(\boldsymbol{x})$ the shape function associated with the node i. As grains are assumed to be spherical or discs in the two-dimensional case, the numerator integral can be decomposed into sub-volumes based using the elements facets to cut the grain [44,45]. Then, to estimate the integral over the overlap, the centroid of each sub-volume is used as the integration point. This choice maintains the volume of the grain and allows the mesh size to be of the same order as the grain size without the need to introduce a additional kernel. Fig. A.21 illustrates the overlap cells generated on the mesh to represent the grains. In the mass conservation equation, the averaged solid velocity is computed similarly to the void fraction, as it is also assumes to be continuous field,

$$(\phi \boldsymbol{v})_i = \frac{\int_\Omega \sum_{j \in \mathcal{P}} H_j(\boldsymbol{x}) \boldsymbol{v}_j \phi_i(\boldsymbol{x}) \mathrm{d}\boldsymbol{x}}{\int_\Omega \phi_i(\boldsymbol{x}) \mathrm{d}\boldsymbol{x}} \tag{A.15}$$

where $\mathcal{P}$ is the set of particles, $H_j(\boldsymbol{x})$ the Heaviside function associated to the particle j and $\boldsymbol{v}_j$ its velocity. The fluid-grain interaction force is computed locally for each grain at the centroid of each sub-volume.

A scheme for zero void fraction

The exact computation of the void fraction allows for zero void fraction in cells. In this case, two critical issues arise:

- the governing equations do not introduce any pressure dependency,

- the drag parametrisation may result in arbitrary large values.

If a naive explicit coupling is considered between the fluid and the solid phase, the governing equations, Eqs. (1)–(2), for zero void fraction reduces to find $\boldsymbol{u}$ an p such that

$$\begin{aligned}
&\boldsymbol{\nabla} \cdot \boldsymbol{v}^n = 0, \\
&\gamma^n \left(\boldsymbol{v}^n - \boldsymbol{u}^{n+1} \right) = \boldsymbol{0},
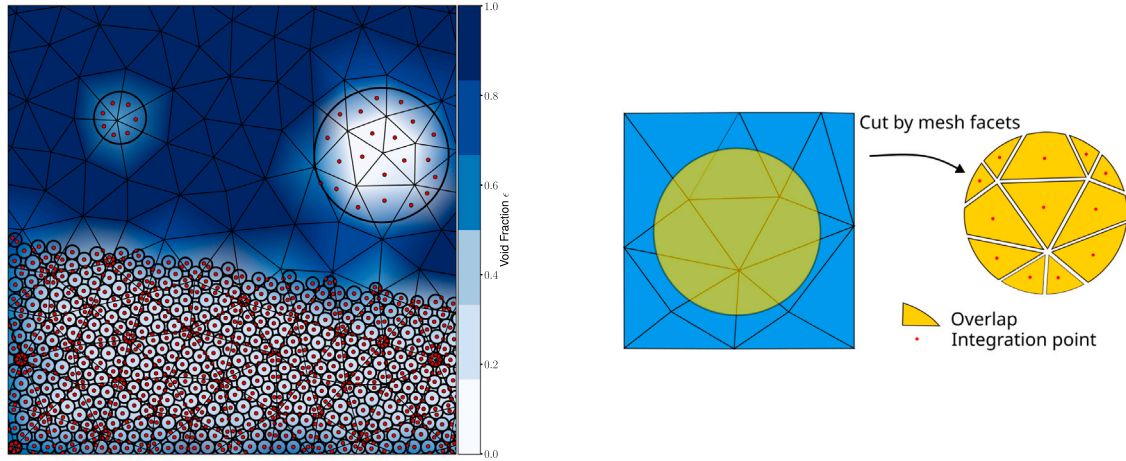\end{aligned} \tag{A.16}$$

Fig. A.21. Representation of the grains on the mesh. On the right, a grain is cut into sub-volumes by the mesh facets. On the left, the volume of each sub-volume is distributed over the mesh nodes to compute the void fraction. The integration point is the centroid of each sub-volume.

where $\boldsymbol{v}$ is the solid mean velocity and γ is the drag force coefficient, $\boldsymbol{u}$ is the fluid velocity and p the pressure field. If the numerical solid velocity field over the mesh is strictly divergence-free, the system becomes under-determined. Otherwise, the mass conservation is never satisfied and the system is impossible. To address these problems, a closure relation is needed between the solid velocity and the pressure field. This is achieved through a semi-implicit estimation of the solid velocity field.

Semi-implicit coupling scheme. Our approach involves predicting the solid velocity field to couple it with the pressure field. The system is

$$\boldsymbol{\nabla} \cdot \boldsymbol{v}^* = 0,$$
$$\gamma^n \left(\boldsymbol{v}^* - \boldsymbol{u}^{n+1} \right) = 0, \tag{A.17}$$

The superscripts n and $n+1$ indicate the time level and $*$ indicates the predicted value. Using grain dynamics, Eq. (6), the solid velocity can be predicted [12]

$$m \frac{\boldsymbol{v}_i^* - \boldsymbol{v}_i^n}{\Delta t} = \boldsymbol{F}_c + m\boldsymbol{g} - V_i \boldsymbol{\nabla} p^{n+1} + \gamma_i^n \left(\boldsymbol{u}_i^{n+1} - \boldsymbol{v}_i^* \right) \tag{A.18}$$

where m_i is the particle mass, Δt is the time step, $\boldsymbol{u}$ is the fluid velocity at the particle position, $\boldsymbol{g}$ is the gravity vector, $\boldsymbol{F}_c$ is the contact force, V_i is the particle volume, and p is the pressure field. By isolating the predicate $\boldsymbol{v}_i^*$, the solid velocity is obtained depending on the pressure gradient

$$\boldsymbol{v}_i^* = \left(\frac{m_i}{\Delta t} + \gamma_i^n \right)^{-1} \left(\frac{m_i}{\Delta t} \boldsymbol{v}_i^n + \gamma_i^n \boldsymbol{u}_i^{n+1} + m_i \boldsymbol{g} + \boldsymbol{F}_c - V_i \boldsymbol{\nabla} p^{n+1} \right). \tag{A.19}$$

A smooth representation is built over the mesh, Eq. (A.15),

$$\boldsymbol{v}_i^* \xrightarrow{\text{(A.15)}} \boldsymbol{v}^* \tag{A.20}$$

To emphasise the pressure dependency, the solid velocity field is decomposed into a pressure gradient term and an extra term, denoted $\boldsymbol{F}$, which depends on the fluid velocity, external forces and the previous solid velocity,

$$\boldsymbol{v}^* = C(\boldsymbol{x})\boldsymbol{\nabla} p^{n+1} + \boldsymbol{F}(\boldsymbol{x}, \boldsymbol{u}^{n+1}, \boldsymbol{v}^n, \boldsymbol{g}, \boldsymbol{F}_c). \tag{A.21}$$

Once the divergence is taken, a pressure diffusive term is obtained.

Bound on the drag coefficient. As noted, the drag coefficient can lead to unphysical results since it is a function of the void fraction and may approach infinity as the void fraction approaches zero. To prevent this, the void fraction is capped at a small value of 10^{-8}.

Appendix B. Non-smooth contact dynamics

Non-smooth contact dynamics is used to model the particle–particle and particle–wall interactions. The dynamics is written in the contact basis where the relative velocity between the two objects is denoted $\mathbf{v}$ and the contact basis generated by the normal vector $\mathbf{n}$ to the tangential surface at the point of contact. Each collision is resolved by finding the impulse $\mathbf{p}$ required to prevent any overlapping at the end of the shock, known as the Signorini condition [46]. As for the tangential reaction, it is modelled by Coulomb's friction law. Each contact must satisfy the following conditions,

$$\begin{array}{ll} \mathbf{v}^+ - \mathbf{v}^- = \mathbf{W}\,\mathbf{p} & \text{Cinematic condition} \\ \left(\mathbf{v}^+ \cdot \mathbf{n} \right) \left(\mathbf{p} \cdot \mathbf{n} \right) = 0, & \text{Signorini condition} \\ \| \mathbf{p} - (\mathbf{p} \cdot \mathbf{n})\mathbf{n} \| \leq \mu \, |\mathbf{p} \cdot \mathbf{n}|, & \text{Coulomb's friction law} \end{array} \tag{B.1}$$

where $\mathbf{v}^-$ and $\mathbf{v}^+$ are the relative velocities before and after the collision and μ is the coefficient of friction. The velocity response to an impulse at the contact point is described by the Delassus operator $\mathbf{W}$. This problem is solved for each contact occurring in the system during a time step Δt. To speed up the convergence of the global problem, the contact network is solved iteratively using a Gauss–Seidel procedure [47]. The resulting contact force density applied to particle i by the contact network, denoted $\boldsymbol{f}_c$, is obtained as

$$\boldsymbol{f}_c = \frac{1}{V} \sum_{j \in \mathcal{P}} \mathbf{p}_{ij} \Delta t \tag{B.2}$$

where V is the particle volume, $\mathcal{P}$ is the set of particles and $\mathbf{p}_{ij}$ is the contact impulse between the i, j particles.

Heat exchange between particles is assumed to be only due to contact conduction, as convection is carried out by the fluid phase and radiation is neglected. Contact conduction depends on the properties of the materials and the force keeping them in contact. At first approximation, the contact heat transfers through the contact is dependent on the exchange surface. However, the contacts dynamics assumed this surface to be zero. An effective contact surface is estimated by the normal reaction of the contact, denoted r_n, assuming elastic particles and smooth surfaces. The contact reaction is related to the contact impulse by the following relation, $r_n \Delta t = \mathbf{p} \cdot \mathbf{n}$. The net contact conduction density q_c submitted to the grain i and the contact conductance between two grains i, j, denoted H_{ij} are obtained as [48–50]

$$q_c = \frac{1}{V} \sum_{j \in \mathcal{P}} H_{ij}(T_i - T_j), \quad H_{ij} = 4k_s \left(\frac{r_n\, d^*}{2\pi L E^*} \right)^{1/4} \tag{B.3}$$

where k_s is the harmonic mean of the solid heat conductivity, r_n is the normal contact reaction between the two grains i, j, L is the cylinder

length, the effective Young's modulus E^*, the effective contact diameter d^* chosen as

$$\frac{1}{k_s} = 2\left(\frac{1}{k_i} + \frac{1}{k_j}\right), \quad \frac{1}{E^*} = \frac{1 - \nu_i^2}{E_i} + \frac{1 - \nu_j^2}{E_j}, \quad \frac{1}{d^*} = \frac{1}{d_i} + \frac{1}{d_j} \quad (B.4)$$

where ν_i is the Poisson's ratio associated with grain i. A boundary contact is assumed to behave like a particle with an infinite radius and an infinite Young's modulus.

Data availability

Data will be made available on request.

References

[1] P. Basu, Circulating Fluidized Bed Boilers: Design, Operation and Maintenance, Springer International Publishing, Cham, 2015, http://dx.doi.org/10.1007/978-3-319-06173-3.

[2] F. Lin, S. Dorbolo, W. Wang, J. Zou, Deep spontaneous penetration of a water droplet into hot granular materials, Phys. Rev. Fluids 7 (3) (2022) 034301.

[3] C. Loha, S. Gu, J. De Wilde, P. Mahanta, P.K. Chatterjee, ChemInform abstract: Advances in mathematical modeling of fluidized bed gasification, Renew. Sustain. Energy Rev. 40 (2014) 688–715, http://dx.doi.org/10.1016/j.rser.2014.07.199.

[4] L. Rueda Villegas, R. Alis, M. Lepilliez, S. Tanguy, A ghost fluid/level set method for boiling flows and liquid evaporation: Application to the Leidenfrost effect, J. Comput. Phys. 316 (2016) 789–813, http://dx.doi.org/10.1016/j.jcp.2016.04.031.

[5] D. Quéré, Leidenfrost dynamics, Annu. Rev. Fluid Mech. 45 (1) (2013) 197–215, http://dx.doi.org/10.1146/annurev-fluid-011212-140709.

[6] N.A. Patankar, P. Singh, D.D. Joseph, R. Glowinski, T.W. Pan, A new formulation of the distributed Lagrange multiplier/fictitious domain method for particulate flows, Int. J. Multiph. Flow 26 (9) (2000) 1509–1524, http://dx.doi.org/10.1016/S0301-9322(99)00100-7.

[7] J. Capecelatro, O. Desjardins, An Euler–Lagrange strategy for simulating particle-laden flows, J. Comput. Phys. 238 (2013) 1–31, http://dx.doi.org/10.1016/j.jcp.2012.12.015.

[8] T.B. Anderson, R. Jackson, Fluid mechanical description of fluidized beds. Equations of motion, Ind. Eng. Chem. Fundam. 6 (4) (1967) 527–539, http://dx.doi.org/10.1021/i160024a007.

[9] A.S. Baumgarten, K. Kamrin, A general fluid–sediment mixture model and constitutive theory validated in many flow regimes, J. Fluid Mech. 861 (2019) 721–764, http://dx.doi.org/10.1017/jfm.2018.914.

[10] Y.Q. Feng, A.B. Yu, Assessment of model formulations in the discrete particle simulation of gas-solid flow, Ind. Eng. Chem. Res. 43 (26) (2004) 8378–8390, http://dx.doi.org/10.1021/ie049387v.

[11] L. Lacaze, J. Bouteloup, B. Fry, E. Izard, Immersed granular collapse: From viscous to free-fall unsteady granular flows, J. Fluid Mech. 912 (2021) A15, http://dx.doi.org/10.1017/jfm.2020.1088.

[12] M. Constant, F. Dubois, J. Lambrechts, V. Legat, Implementation of an unresolved stabilised FEM–DEM model to solve immersed granular flows, Comput. Part. Mech. (2018) http://dx.doi.org/10.1007/s40571-018-0209-4.

[13] Geitani, A high-order stabilized solver for the volume averaged Navier-Stokes equations, Internat. J. Numer. Methods Fluids (2023) Wiley Online Library, https://onlinelibrary.wiley.com/doi/full/10.1002/fld.5182.

[14] K. Walayat, Z. Wang, K. Usman, M. Liu, An efficient multi-grid finite element fictitious boundary method for particulate flows with thermal convection, Int. J. Heat Mass Transfer 126 (2018) 452–465, http://dx.doi.org/10.1016/j.ijheatmasstransfer.2018.05.007.

[15] CFD-DEM Simulation of Heat Transfer in Fluidized Beds: Model Verification, Validation, and Application | Elsevier Enhanced Reader. http://dx.doi.org/10.1016/j.ces.2018.12.031.

[16] W.E. Ranz, Evaporation from drops-I and-II, 1952, pp. 141–146, 48.

[17] I.C. Kemp, R.E. Bahu, H.S. Pasley, Model development and experimental studies of vertical pneumatic conveying dryers, Dry. Technol. (2007) http://dx.doi.org/10.1080/07373939408961008.

[18] Z. Wang, M. Liu, Semi-resolved CFD–DEM for thermal particulate flows with applications to fluidized beds, Int. J. Heat Mass Transfer 159 (2020) 120150.

[19] J. Li, D. Mason, A computational investigation of transient heat transfer in pneumatic transport of granular particles, Powder Technol. 112 (3) (2000) 273–282, http://dx.doi.org/10.1016/S0032-5910(00)00302-8.

[20] N. Wakao, T. Funazkri, Effect of fluid dispersion coefficients on particle-to-fluid mass transfer coefficients in packed beds: Correlation of sherwood numbers, Chem. Eng. Sci. 33 (10) (1978) 1375–1384, http://dx.doi.org/10.1016/0009-2509(78)85120-3.

[21] A.V. Patil, E.A.J.F. Peters, J.A.M. Kuipers, Comparison of CFD–DEM heat transfer simulations with infrared/visual measurements, Chem. Eng. J. 277 (2015) 388–401, http://dx.doi.org/10.1016/j.cej.2015.04.131.

[22] M. Constant, N. Coppin, F. Dubois, V. Vidal, V. Legat, J. Lambrechts, Simulation of air invasion in immersed granular beds with an unresolved FEM–DEM model, Comput. Part. Mech. (2020) http://dx.doi.org/10.1007/s40571-020-00351-4.

[23] M. Constant, N. Coppin, F. Dubois, R. Artoni, J. Lambrechts, V. Legat, Numerical investigation of the density sorting of grains using water jigging, Powder Technol. 393 (2021) 705–721.

[24] N. Coppin, M. Henry, M. Cabrera, E. Azéma, F. Dubois, V. Legat, J. Lambrechts, Collapse dynamics of two-dimensional dry and immersed granular columns of elongated grains, Phys. Rev. Fluids 8 (9) (2023) 094303.

[25] N. Coppin, M. Constant, J. Lambrechts, F. Dubois, V. Legat, Numerical analysis of the drag on a rigid body in an immersed granular flow, in: Particles 2021, Hamburg, 2021.

[26] M. Jean, V. Acary, Y. Monerie, Non-smooth Contact Dynamics approach of cohesive materials, Phil. Trans. R. Soc. A 359 (2001) 2497–2518, http://dx.doi.org/10.1098/rsta.2001.0906.

[27] Z. Zhou, S. Kuang, K. Chu, A. Yu, Discrete particle simulation of particle–fluid flow: model formulations and their applicability, J. Fluid Mech. 661 (2010) 482–510.

[28] Y. Feng, A. Yu, Assessment of model formulations in the discrete particle simulation of gas- solid flow, Ind. Eng. Chem. Res. 43 (26) (2004) 8378–8390.

[29] A.D. Colburn, Analogy of mass transfer, 1933, p. 174, 29.

[30] Z. Duan, Y. Duan, Sphere drag and heat transfer, Sci. Rep. 5 (2015) http://dx.doi.org/10.1038/srep12304.

[31] R. Di Felice, The voidage function for fluid-particle interaction systems, Int. J. Multiph. Flow 20 (1) (1994) 153–159, http://dx.doi.org/10.1016/0301-9322(94)90011-6.

[32] W.C. Y, Mechanics of fluidization, in: Fluid Particle Technology, Chem. Eng. Progress. Symposium Series, Vol. 62, 1966, pp. 100–111.

[33] J.M. DallaValle, A. Klemin, Micromeritics: The Technology of the Particles, Pitman Publishing Corporation, New York ; Chicago, 1943.

[34] J.D. Acetis, G. Thodos, Mass and heat transfer in flow of gases through spherical packings, ACS Publ. (2002) http://dx.doi.org/10.1021/ie50612a026, https://pubs.acs.org/doi/pdf/10.1021/ie50612a026.

[35] W. Komarnicky, Effect of Packing Geometry on Heat and Mass Transfer in Stacked Beds of Spheres (Ph.D. thesis), University of British Columbia, 1956, http://dx.doi.org/10.14288/1.0059067.

[36] G.F. Malling, G. Thodos, Analogy between mass and heat transfer in beds of spheres: Contributions due to end effects, Int. J. Heat Mass Transfer 10 (4) (1967) 489–498, http://dx.doi.org/10.1016/0017-9310(67)90169-X.

[37] A.S. Gupta, G. Thodos, Mass and heat transfer in the flow of fluids through fixed and fluidized beds of spherical particles, A.I.Ch.E. (Am. Inst. Chem. Eng.) J. 8 (1962) http://dx.doi.org/10.1002/aic.690080509.

[38] C.R. Wilke, O. Hougen, Mass transfer in the flow of gases through granular solids extended to low modified Reynolds numbers, Trans. Am. Inst. Chem. Eng. 41 (4) (1945) 445–451.

[39] S.C. N, Simultaneous heat and mass transfer in a duffusion-controlled chemical reaction ; Part II : Studies in a packed bed, Chem. Eng. Prog. 50 (1954) 504–510.

[40] J. Yang, J. Wang, S. Bu, M. Zeng, Q. Wang, A. Nakayama, Experimental analysis of forced convective heat transfer in novel structured packed beds of particles, Chem. Eng. Sci. 71 (2012) 126–137, http://dx.doi.org/10.1016/j.ces.2011.12.005.

[41] Shapes and Velocities of Single Drops and Bubbles Moving Freely through Immisicible Liquids | CiNii Research. https://cir.nii.ac.jp/crid/1573105974966585984.

[42] C. Voivret, F. Radjai, J.-Y. Delenne, M.S. El Youssoufi, Space-filling properties of polydisperse granular media, Phys. Rev. E 76 (2) (2007) 021301.

[43] F.Z. El Korchi, F. Jamin, M.S. El Youssoufi, Etude expérimentale à l'échelle locale de la coalescence de ponts capillaires dans les sols granulaires, in: 35èmes Rencontres Universitaires de Génie Civil, in: Actes Des 35èmes Rencontres Universitaires de Génie Civil, Nantes, France, 2017.

[44] D.A. Clarke, A.J. Sederman, L.F. Gladden, D.J. Holland, Investigation of void fraction schemes for use with CFD-DEM simulations of fluidized beds, Ind. Eng. Chem. Res. 57 (8) (2018) 3002–3013.

[45] S. Strobl, A. Formella, T. Pöschel, Exact calculation of the overlap volume of spheres and mesh elements, J. Comput. Phys. 311 (2016) 158–172.

[46] F. Radjaï, F. Dubois, Modélisation numérique discrète des matériaux granulaires. 459.

[47] F. Dubois, V. Acary, M. Jean, The contact dynamics method: A nonsmooth story, C. R. Mécanique 346 (3) (2018) 247–262, http://dx.doi.org/10.1016/j.crme.2017.12.009.

[48] M.M. Yovanovich, Thermal contact resistance across elastically deformed spheres, J. Spacecr. Rockets 4 (1) (1967) 119–122, http://dx.doi.org/10.2514/3.28821.

[49] A. Bejan, A.D. Kraus, Heat Transfer Handbook, John Wiley & Sons, 2003.

[50] G.K. Batchelor, R.W. O'brien, Thermal or electrical conduction through a granular material, Proc. R. Soc. A 355 (1682) (1977) 313–333.